Journal of Pharmaceutical Analysis 14 (2024) 100971

Contents lists available at ScienceDirect

Journal of Pharmaceutical Analysis

journal homepage: www.elsevier.com/locate/jpa

Original article

Spatially resolved metabolomics visualizes heterogeneous distribution of metabolites in lung tissue and the anti-pulmonary fibrosis effect of *Prismatomeris connate* extract

Haiyan Jiang [a, 1], Bowen Zheng [b, 1], Guang Hu [c], Lian Kuang [a], Tianyu Zhou [d], Sizheng Li [a], Xinyi Chen [b], Chuangjun Li [b], Dongming Zhang [b], Jinlan Zhang [b], Zengyan Yang [e], Jiuming He [b, f, **], Hongtao Jin [a, f, g, *]

[a] *New Drug Safety Evaluation Center, Institute of Materia Medica, Chinese Academy of Medical Sciences & Peking Union Medical College, Beijing, 100050, China*
[b] *State Key Laboratory of Bioactive Substance and Function of Natural Medicines, Institute of Materia Medica, Chinese Academy of Medical Sciences & Peking Union Medical College, Beijing, 100050, China*
[c] *School of Biomedical Sciences, Hunan University, Changsha, 410082, China*
[d] *College of Pharmacy, Shaanxi University of Traditional Chinese Medicine, Xianyang, Shaanxi, 712046, China*
[e] *Guangxi International Zhuang Medicine Hospital, Nanning, 530201, China*
[f] *Key Laboratory for Safety Research and Evaluation of Innovative Drug, National Medical Products Administration, Beijing, 102206, China*
[g] *Beijing Union-Genius Pharmaceutical Technology Development Co., Ltd., Beijing, 100176, China*

ARTICLE INFO

Article history:
Received 9 November 2023
Received in revised form
22 February 2024
Accepted 25 March 2024
Available online 27 March 2024

Keywords:
Spatially resolved metabolomics
Mass spectrometry imaging
Network pharmacology
Pulmonary fibrosis
Prismatomeris connate extract

ABSTRACT

Pulmonary fibrosis (PF) is a chronic progressive end-stage lung disease. However, the mechanisms underlying the progression of this disease remain elusive. Presently, clinically employed drugs are scarce for the treatment of PF. Hence, there is an urgent need for developing novel drugs to address such diseases. Our study found for the first time that a natural source of *Prismatomeris connata* Y. Z. Ruan (Huang Gen, HG) ethyl acetate extract (HG-2) had a significant anti-PF effect by inhibiting the expression of the transforming growth factor beta 1/suppressor of mothers against decapentaplegic (TGF-β1/Smad) pathway. Network pharmacological analysis suggested that HG-2 had effects on tyrosine kinase phosphorylation, cellular response to reactive oxygen species, and extracellular matrix (ECM) disassembly. Moreover, mass spectrometry imaging (MSI) was used to visualize the heterogeneous distribution of endogenous metabolites in lung tissue and reveal the anti-PF metabolic mechanism of HG-2, which was related to arginine biosynthesis and alanine, asparate and glutamate metabolism, the downregulation of arachidonic acid metabolism, and the upregulation of glycerophospholipid metabolism. In conclusion, we elaborated on the relationship between metabolite distribution and the progression of PF, constructed the regulatory metabolic network of HG-2, and discovered the multi-target therapeutic effect of HG-2, which might be conducive to the development of new drugs for PF.

1. Introduction

Pulmonary fibrosis (PF) is a terminal disease characterized by alveolar epithelial cell injury, extracellular matrix (ECM) collagen deposition, and enhanced activation and proliferation of fibroblasts/myofibroblasts, combined with inflammatory damage and tissue structure destruction [1]. Clinically, PF mainly manifests as idiopathic PF (IPF) with a median survival of 3–5 years after diagnosis [2]. Currently, only pirfenidone and nintedanib are approved for the treatment of IPF [3], but both of the drugs cannot reverse or prevent the progression of PF [4,5]. In addition, adverse drug reactions involving the hepatobiliary, cardiovascular, gastrointestinal,

* Corresponding author. New Drug Safety Evaluation Center, Institute of Materia Medica, Chinese Academy of Medical Sciences & Peking Union Medical College, Beijing, 100050, China.
** Corresponding author. State Key Laboratory of Bioactive Substance and Function of Natural Medicines, Institute of Materia Medica, Chinese Academy of Medical Sciences & Peking Union Medical College, Beijing, 100050, China.
E-mail addresses: jinhongtao@imm.ac.cn (H. Jin), hejiuming@imm.ac.cn (J. He).
[1] Both authors contributed equally to this work.

https://doi.org/10.1016/j.jpha.2024.100971

and dermatologic systems may occur in the early stages of drug administration [6], and the high costs of the drugs causes substantial economic burdens to patients [7]. Therefore, it is urgent to find new therapeutic drugs that can effectively prevent and treat IPF.

Fibrosis begins at the periphery of the lung and progresses to the center. The heterogeneous mechanical tension induced by respiratory movement acts on alveolar stem cells and induces the heterogeneous transforming growth factor-beta (TGF-β) pathway that drives the development of PF originating at the margins of the lung lobe [8]. Those findings verified the correlation between lung tissue structure and the pathogenesis of fibrosis through the classical signaling pathway. However, the fibrotic process is driven by multiple factors and pathways, forming a systematic and complex molecular network. Metabolomics provides a new research perspective for the mechanism of PF disease and fibrometabolism is a developing and arousing avenue of research [9]. Dysregulation of glycolysis, glutamine metabolism, and lipid metabolism have been shown to promote the pathophysiological process of fibrosis [9–11]. Recently, spatially resolved metabolomics approaches based on mass spectrometry imaging (MSI) technology have facilitated qualitative, quantitative, and positioning analyses of metabolites simultaneously. The characterization of the spatial distribution of metabolites can deepen the understanding of lung tissue structure and physiological activities, and further elucidate the relationships between the pathophysiological processes of PF and the changes in the spatial heterogeneity and abundance of metabolites. Such details will, thus, contribute to clarifying the complex multi-cellular interactions driving organ fibrosis.

The root of *Prismatomeris connata* Y. Z. Ruan (Huang Gen, HG) is a characteristic medicinal material in Guangxi Zhuang autonomous region, China. It has the effects of cooling blood, stopping bleeding, removing dampness, and eliminating jaundice, which is used for the treatment of early-stage silicosis. There are few studies on the compositional analysis and pharmacological mechanisms of HG. The main components of HG have been identified, including anthraquinones, tetrahydroanthraquinones, long-chain fatty acids (FAs), alkenes (aldehydes), long-chain alkanes, organoaluminum, and polysaccharides [12,13]. Studies have shown that 3-hydroxy-1,5,6-trimethoxy-2-methyl-9,10-anthraquinone,4-hydroxy-1,2,3-trimethoxy-7-hydroxymethylanthracene-9,10-dione extracted from HG are active against non-small cell lung carcinoma [14,15]. It was found that the HG alcohol extract and its monomer, scopoletin, had anti-hepatic fibrosis activity in mice and promote the apoptosis of hepatic astrocytes [16–18]. However, whether HG extract has anti-PF activity has not been reported.

Therefore, we evaluated the therapeutic effects of HG extracts (HG-2, HG-3, and HG-4) on PF using a bleomycin (BLM)-induced mouse model and found that HG-2 can significantly improve PF in mice through the TGF-β1/suppressor of mothers against decapentaplegic (Smad) signaling pathway. Given that HG-2 is a component of traditional Chinese medicine (TCM), we further analyzed the main components in HG-2 by ultra-high-performance liquid chromatography coupled with quadrupole time-of-flight tandem mass spectrometry (UHPLC-QTOF-MS/MS) and performed network pharmacology analyses based on the detected compounds. Meanwhile, we used ambient fluid desorption electrospray ionization (AFADESI)-MSI to visualize the spatial distribution of endogenous metabolites in lung tissue and explore the potential metabolic mechanism of HG-2 in improving PF based on spatially resolved metabolomics. This work will enhance the understanding of metabolic regulation in PF disease and provide reference for the development of multi-target new drugs.

2. Materials and methods

2.1. Materials and reagents

The BLM sulfate was provided by Zhejiang Hisun Pharmaceutical Co., Ltd. (Taizhou, China). Phosphate-buffered saline (PBS) solution was purchased from Beyotime Biotechnology Inc. (Shanghai, China). The bovine serum albumin (BSA) was obtained from Sigma-Aldrich (St. Louis, MO, USA). The 3,3′-diaminobenzidine (DAB) chromogenic kit and rabbit two-step kit were obtained from Zhongshan Jinqiao Biotechnology Co., Ltd. (Beijing, China). Masson staining kit and enzyme-linked immunosorbent assay (ELISA) kit of hydroxyproline and TGF-β1 were obtained from Nanjing Jiancheng Bioengineering Institute (Nanjing, China). The radio immunoprecipitation assay (RIPA) lysis buffer and bicinchoninic acid (BCA) protein assay kit were obtained from Thermo Fisher Scientific Inc. (Waltham, MA, USA). The RNA-Quick Purification Kit was purchased from Yishan Biotechnology Co., Ltd. (Shanghai, China). The TransScript Fly First-Strand complementary DNA (cDNA) Synthesis SuperMix was obtained from TransGen Biotech Inc. (Beijing, China). The KAPA SYBR FAST Universal qPCR Kit was purchased from KAPA Biosystems (Boston, MA, USA). The primary antibodies, including anti-α-smooth muscle actin (anti-α-SMA), anti-collagen type l alpha 1 chain (anti-COL1A1), anti-Smad2/3, anti-p-Smad2/3, anti-glyceraldehyde 3-phosphate dehydrogenase (anti-GAPDH), and horseradish peroxidase-conjugated secondary antibody were provided by Cell Signaling Technology (Boston, MA, USA). The enhanced chemiluminescence (ECL) solution was obtained from Tianon Biotech. Inc. (Shanghai, China). Liquid chromatography(LC)-MS grade acetonitrile and methanol were purchased from Thermo Fisher Scientific Inc.

2.2. HG extract preparation

HG was collected at Fangcheng in Guangxi Zhuang autonomous region, China, and was identified by Associate Chief Pharmacist, Richun Lan from Guangxi Institute of Ethnic Medicine (Nanning, China). The HG extracts were provided by Associate Chief Pharmacist, Zengyan Yang from Guangxi International Zhuang Medical Hospital (Nanning, China). The specific preparation method was as follows. After the HG was cleaned, dried, and crushed into coarse powder, 20 kg of powder was weighed and divided into a multifunctional extraction concentrator (Zhongxiang Light Industrial Machinery Factory, Wenzhou, China). A total of 140 kg of 95% ethanol was added according to a material-to-liquid ratio of 1:7, soaked at room temperature for 1 h, heated and reflowed for 1 h, filtered with a 350-mesh filter cloth, pumped into a liquid storage tank, and vacuumed to a concentration tank for concentrating. After three extractions using 140 kg of 95% ethanol, the filtrates were combined and concentrated until a thick extract (1.25 kg) was obtained. The thick extract was dissolved with an appropriate amount of distilled water, and then extracted and evaporated with petroleum ether, ethyl acetate, and *n*-butanol. A total of 56 g of HG petroleum ether extract (HG-1; yield: 4.48%), 169 g of HG ethyl acetate extract (HG-2; yield: 13.52%), 237 g of HG normal alcohol extract (HG-3; yield: 18.96%), and 574 g of HG water extract (HG-4; yield: 45.92%) [19] was obtained.

2.3. Animals and experimental design

Male specific pathogen free (SPF) C57BL/6N mice weighing 18–22 g were purchased from Beijing Vital River Laboratory Animal Technological Company (Beijing, China) (License No.: SCXK-(Jing) 2016-0011). Mice were raised in the SPF Experimental Animal

Center, New Drug Safety Evaluation Center, Institute of Materia Medica, Chinese Academy of Medical Sciences & Peking Union Medical College (Beijing, China), with a room temperature of 25 ± 2 °C, a humidity of 60% ± 5%, and a 12-h light/dark cycle. The mice had free access to a standard diet and water. The experimental protocol was approved by the Animal Welfare Ethics Committee of the New Drug Safety Evaluation Center, Institute of Materia Medica, Chinese Academy of Medical Sciences & Peking Union Medical College (Beijing, China) (Approval Nos.: 000026 and 0000268).

The mice were randomly divided into six groups (n = 15): control, model (BLM), nindanib (BLM + nindanib, 50 mg/kg), HG-2 (BLM + HG-2, 100 mg/kg), HG-3 (BLM + HG-3, 100 mg/kg), and HG-4 (BLM + HG-4, 100 mg/kg). PF was established in mice by single-dose intratracheal administration of 2 U/kg of BLM sulfate in 50 μL of sterile PBS. The mice in the control group were treated with the same volume of sterile PBS. Fourteen days after modeling, the control and model groups were given 0.5% carboxymethyl cellulose sodium (CMC-Na), while the other groups were given HG extracts by intragastric administration for 14 days, with an administration volume of 10 mL/kg. During the experiment, relevant indicators were observed and recorded, including body weight, death, physiological activities, and behavioral patterns.

The mice were randomly divided into six groups (n = 15): control, model (BLM), nintedanib (BLM + nintedanib, 50 mg/kg), low-dose HG-2 (BLM + HG-2, 50 mg/kg), medium-dose HG-2 (BLM + HG-2, 100 mg/kg), and high-dose HG-2 (BLM + HG-2, 200 mg/kg). The mice were treated with BLM (2 U/kg) to induce PF, while the mice were intratracheally instilled with sterile PBS as the control group. The control and model groups were given 0.5% CMC-Na, while the other groups were given HG-2 at specific doses by intragastric administration for 14 days, with an administration volume of 10 mL/kg.

2.4. Pulmonary function tests

Mice were anesthetized by intraperitoneal injection of pentobarbital sodium (90 mg/kg) within 24 h after the last administration. Mice were surgically connected to endotracheal tubes and the FlexiVent pulmonary system (SCIREQ, Montreal, Canada). The inspiratory capacity (IC) of mice was detected by the Deep Inflation module, including resistance, compliance (Crs), elastance, central airway resistance, tissue damping, and tissue elasticity.

2.5. Histological analysis

After collecting the lungs, the tissues were fixed with 4% paraformaldehyde, embedded in paraffin, and made into 3-μm sections. Hematoxylin and eosin (HE) stainings was used for histopathological examination. Tissue sections were deparaffinized and rehydrated, then subjected to HE and Masson staining for histological analysis. HE scoring was based on the total extent of fibroplasia. Scoring criteria: no fibrous hyperplasia area, grade 0; fibrous hyperplasia area < 10%, grade 1; fibrous hyperplasia area < 25%, grade 2; fibrous hyperplasia area < 50%, grade 3; fibrous hyperplasia area < 75%, grade 4; and fibrous hyperplasia area > 75%, grade 5. Masson staining was used to characterize collagen deposition and assess the degree of fibrosis by calculating the percentage of positive areas of blue collagen fibers in random visual fields. The percentage of positive area was quantitatively analyzed using ImageJ software (National Institutes of Health (NIH), Bethesda, MD, USA).

2.6. Immunohistochemistry

The rabbit two-step kit was used for immunohistochemical analysis to detect the distribution of α-SMA in lung tissue. Sections were deparaffinized and hydrated. Antigen retrieval was performed with 0.01 M citrate buffer. Endogenous peroxidases were quenched with 3% H_2O_2 for 15 min and subsequently blocked with 5% BSA for 15 min. The sections were then incubated with α-SMA antibody at 4 °C overnight. After washing with PBS, the sections were incubated with horseradish peroxidase-conjugated secondary antibodies for 1 h at room temperature. The DAB chromogenic kit was added to the sections to reveal the tan-positive area and then the slides were sealed and examined under the Axio Vert Al inverted microscope (Carl Zeiss, Jena, Germany). The relative areas of positive expression were quantitatively analyzed using ImageJ software and at least 10 high-power fields within each lung section were evaluated.

2.7. Hydroxyproline and inflammatory factor assays

The lung tissues were collected and frozen at −80 °C. The supernatant was collected after the lung tissue was fully homogenized in PBS, and detected according to the kit instructions for hydroxyproline and TGF-β1.

2.8. Western blot assays

The lung tissues were homogenized in RIPA lysis buffer containing 1% protease and phosphatase inhibitor and lysed on ice for 30 min. The supernatant was obtained by centrifugation at 12,000 *g* for 20 min at 4 °C, and the protein concentration of the sample was measured using the BCA protein assay kit. The proteins in the sample were separated on 10% sodium dodecyl sulfate-polyacrylamide gel electrophoresis (SDS-PAGE) and polyvinylidene fluoride (PVDF) membranes. The 5% BSA was used as the blocking solution for phosphorylated antibodies, and 5% fat-free milk was used as a blocking solution for all other antibodies. The samples were shaken at room temperature for 1 h in blocking solution and then incubated overnight at 4 °C with primary antibodies, including anti-α-SMA, anti-COL1A1, anti-Smad2/3, anti-p-Smad2/3, and anti-GAPDH. All antibodies were diluted 1:1,000. After washing the membrane, samples were incubated with the corresponding enzyme-linked secondary antibodies at room temperature for 1 h, and visualized using ECL solution with an ImageQuant LAS 4000 gel imaging system (General Electric Company, Fairfield, MA, USA).

2.9. Composition analysis

HG-2 was accurately weighed at 3.0 mg and transferred to a 1.5 mL Eppendorf tube with 1 mL of ethyl acetate:isopropyl alcohol (3:7, *V/V*). The mixture was dissolved by vortex and then centrifugated at 12,000 r/min for 10 min. The sample was diluted to 1 mg/mL with ethyl acetate:isopropyl alcohol (3:7, *V/V*) for injection analysis.

The Agilent 1290 series UHPLC system combined with an Agilent 6550 Q-TOF/MS instrument was used for compositional analysis. The Agilent 1290 series UHPLC system (Agilent Technologies, Santa Clara, CA, USA) was also used for chromatographic analysis. All samples were detected using an ethylene bridged hybrid (BEH) C_{18} column (2.1 mm × 100 mm, 1.7 μm; Waters, Milford, MA, USA) at 4 °C. The column temperature was 30 °C. The mobile phase was water (A, 0.1% formic acid, 1 mmol/L ammonium acetate) and acetonitrile (B, 0.1% formic acid, 1 mmol/L ammonium acetate). The flow rate of the mobile gradient phase was 0.3 mL/min. The column temperature was 30 °C. The gradient elution condition was optimized as follows: 0−5 min, 20% B and 5−30 min, 20%−100% B.

An Agilent 6550 Q-TOF/MS instrument (Agilent Technologies) was used for MS and the MS conditions were as follows: the gas

temperature was maintained at 280 °C and the gas flow rate was 11 L/min. The sheath gas temperature was 325 °C with a flow of 12 L/min. The mass scan range of MS was *m/z* 150–1,200 and the mass scan range of MS/MS was *m/z* 50–1,200. The collision energy in MS/MS was 10, 20, 30, 40, and 50 V.

2.10. Network pharmacological analysis

Based on the analysis and identification of HG-2 components, the SwissTargetPrediction database (http://www.swisstargetprediction.ch/) was used to search for potential targets of HG-2 components. The keywords "pulmonary fibrosis" or "lung fibrosis" were entered in Online Mendelian Inheritance in Man (OMIM) (https://omim.org/). The GeneCards (https://www.genecards.org/) database was used to screen-out the potential disease targets. All gene targets were standardized through the UniProt database (http://www.uniProt.org/). The "drug-ingredient-target-disease" network was constructed using Cytoscape 3.7.0 software (http://cytoscape.org). The gene targets were introduced into the STRING database (https://string-db.org/) to obtain the protein-protein interaction (PPI) data, which were then imported into Cytoscape 3.7.0 to establish the PPI network. Then, the Database for Annotation, Visualization and Integrated Discovery (DAVID) online tool (https://david.ncifcrf.gov/) was applied to the Gene Ontology (GO) enrichment analysis and the Kyoto Encyclopedia of Genes and Genomes (KEGG) pathway enrichment analysis.

Molecular docking was used to evaluate the interaction strength of target proteins and compounds. The three-dimensional (3D) structure of target proteins was obtained from the Protein Data Bank (PDB) database (http://www1.rcsb.org/). Subsequently, the core components were drawn in 2D structure using ChemBio Ultra 14.0 software (PerkinElmer, Waltham, MA, USA), converted into a 3D structure and adjusted to the spatial conformation to minimize the energy using Chem3D software (PerkinElmer). Autodock 1.5.6 software (https://autodock.scripps.edu/) was used to simulate the binding mode of the compound and target protein and scan the binding site using the lowest energy. Finally, PyMOL 2.5 software (https://pymol.org/2/) was utilized to visualize the optimal conformation of the binding site for both the compounds and proteins.

2.11. Quantitative real-time polymerase chain reaction (qRT-PCR)

Total RNA was extracted from lung tissue samples using the RNA Quick Purification Kit (Yishan Biotechnology Co., Ltd.). cDNA was obtained by RNA reverse transcription using the TransScript Fly First-Strand cDNA Synthesis SuperMix (TransGen Biotech) and a T100™ PCR thermal cycler (Bio-Rad, Hercules, CA, USA). *GAPDH* was the internal standard. The primer sequences of matrix metalloproteinase 2 (*MMP2*), fibroblast growth factor receptor 1 (*FGFR1*), platelet-derived growth factor receptor alpha (*PDGFRA*), *PDGFRB*, Jun proto-oncogene (*JUN*), prostaglandin-endoperoxide synthase 2 (*PTGS2*), signal transducer and activator of transcription 3 (*STAT3*), and mitogen-activated protein kinase 1 (*MAPK1*) are listed in Table S1. The KAPA SYBR FAST Universal qPCR Kit was used for RT-qPCR in an ABI Prism 7900HT Fast Real-Time PCR System (Thermo Fisher Scientific Inc.).

2.12. MSI analysis

The lung tissue was embedded in an optimal cutting temperature compound (Leica, Wetzlar, Germany) and sliced into 12-μm thick sections using a Leica CM1860 cryostat (Leica) at −20 °C. The slices were transferred to a positive charge desorption plate and desiccated at −20 °C for 1 h and then at room temperature for 2 h before MSI analysis.

The AFADESI-MSI system was used for mass spectral data acquisition, which consisted of an AFADESI ambient ion source and a Q-Orbitrap mass spectrometer (Q-Exactive, Thermo Fisher Scientific Inc.) [20,21]. The tissue sections were fixed on an electrical moving stage (MTS225, Beijing Optical Instrument Factory, Beijing, China), which moved at a horizontal speed of 0.2 mm/s, and a vertical step size of 0.2 mm. The parameters of AFADESI-MSI were as follows: MS mode, positive and negative full scan; solvent, acetonitrile:water (8:2, *V/V*; 5 mL/min); spray voltage, 7,000 V; spray gas pressure, 0.7 MPa; scan range, 100–1,000 Da; extraction gas flow, 45 L/min; resolution, 70,000; and capillary temperature, 350 °C.

Mass spectra data were imported into MassImager 2.0 software (Chemmind Technologies Co., Ltd., Beijing, China) for image reconstruction, background subtraction, and data extraction. MarkView™ software 1.2.1 (AB SCIEX, Toronto, Ontario, Canada) was used for peak picking, peak alignment, isotope removal, and normalization. SIMCA-P 14.1 software (Umetrics, Umea, Sweden) was used for the multivariate statistical analysis of variables. The metabolic candidates were selected based on variable importance in projection (VIP) values (threshold > 1), *P* values (threshold < 0.05), fold change (FC) values (threshold > 1.2 or < 0.8), and imaging effects (intensity > 1,000). The selected ions were initially identified according to their accurate masses in METLIN (http://metlin.scripps.edu/), LIPID MAPS (https://www.lipidmaps.org/), and The Human Metabolome Database (HMDB) (http://www.hmdb.ca/), and further identified by comparing the MS/MS fragments with the standard spectra in databases, such as METLIN, HMDB, and mzCloud (https://www.mzcloud.org/). The MetaboAnalyst 5.0 website (http://www.metaboanalyst.ca/) was used for metabolite enrichment analyses.

2.13. Statistical analysis

Statistical analyses were performed using GraphPad Prism 7.0 and Excel 2010. The Shapiro-Wilk test was used to confirm that the data were normally distributed. The statistical differences of all the data were performed by the two-tailed unpaired Student's *t*-test (two groups) or the one-way analysis of variance (ANOVA) (≥2 groups). *P* values < 0.05 were considered to be statistically significant.

3. Results

3.1. HG extracts can improve the characterization of BLM-induced PF in mice

The BLM-induced PF mouse model was established to evaluate the anti-fibrotic activity of extracts from different sections of HG (Fig. 1A). After intratracheal instillation of BLM, the body weight of mice gradually decreased and reached the lowest level after 14 days. After randomization, there was no significant difference in the body weights between the treatment groups (HG-2, HG-3, and HG-4; 100 mg/kg) and the model group. Without drug intervention, the morality rate of animals in the model group was approximately 20%. After 14 days, the body weights of mice in each HG administration group increased compared with the model group (Fig. 1B). HG extracts could also reduce animal mortality. At the end of the experiment, the survival rate of the HG-2 group was significantly higher than that of the model group (Fig. 1C).

After restrictive ventilatory dysfunction such as PF occurs in mice, the main manifestation is limited alveolar expansion during inspiration, resulting in hypoventilation. The FlexiVent system was used to detect the lung function indicators in mice. The results showed that the IC and Crs in the respiratory system of the model

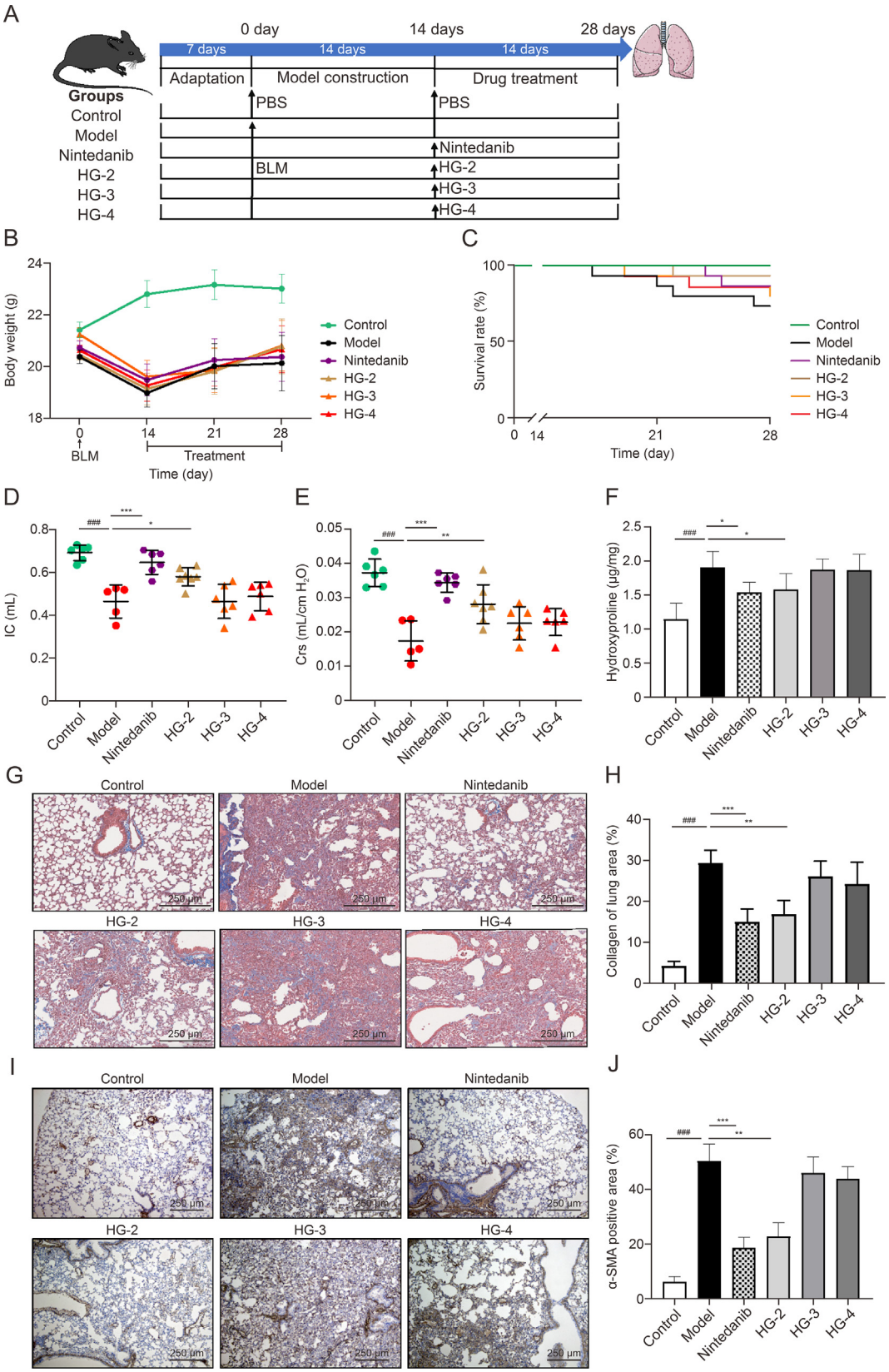

Fig. 1. Effect of different *Prismatomeris connata* Y. Z. Ruan (Huang Gen, HG) extracts on pulmonary fibrosis (PF) in mice. (A) Schematic diagram of animal modeling and administration. (B) Body weight of mice treated with bleomycin (BLM) and HG extract. Animal weight was measured weekly after BLM injection. (C) Survival rate was calculated at the same time point as body weight. (D, E) Respiratory function was measured 14 days after the HG extracts were administered. Inspiratory capacity (IC) (D) and compliance (Crs) (E) were detected by FlexiVent to evaluate the fibrotic changes in the lungs. (F) Quantitative detection of hydroxyproline in right lung tissue. (G, H) Representative images of lung tissue following Masson staining (G) and the percentage of collagen of lung area (H). (I, J) Immunohistochemistry analysis of α-smooth muscle actin (α-SMA) expression in lung sections (I) and the ratio of the α-SMA-positive area to the total area (J). All data are expressed as the mean ± standard deviation (SD) ($n = 5–7$ per group). $^{###}P < 0.001$, compared to the control group; $^{*}P < 0.05$, $^{**}P < 0.01$, and $^{***}P < 0.001$, compared to the model group. PBS: phosphate-buffered saline.

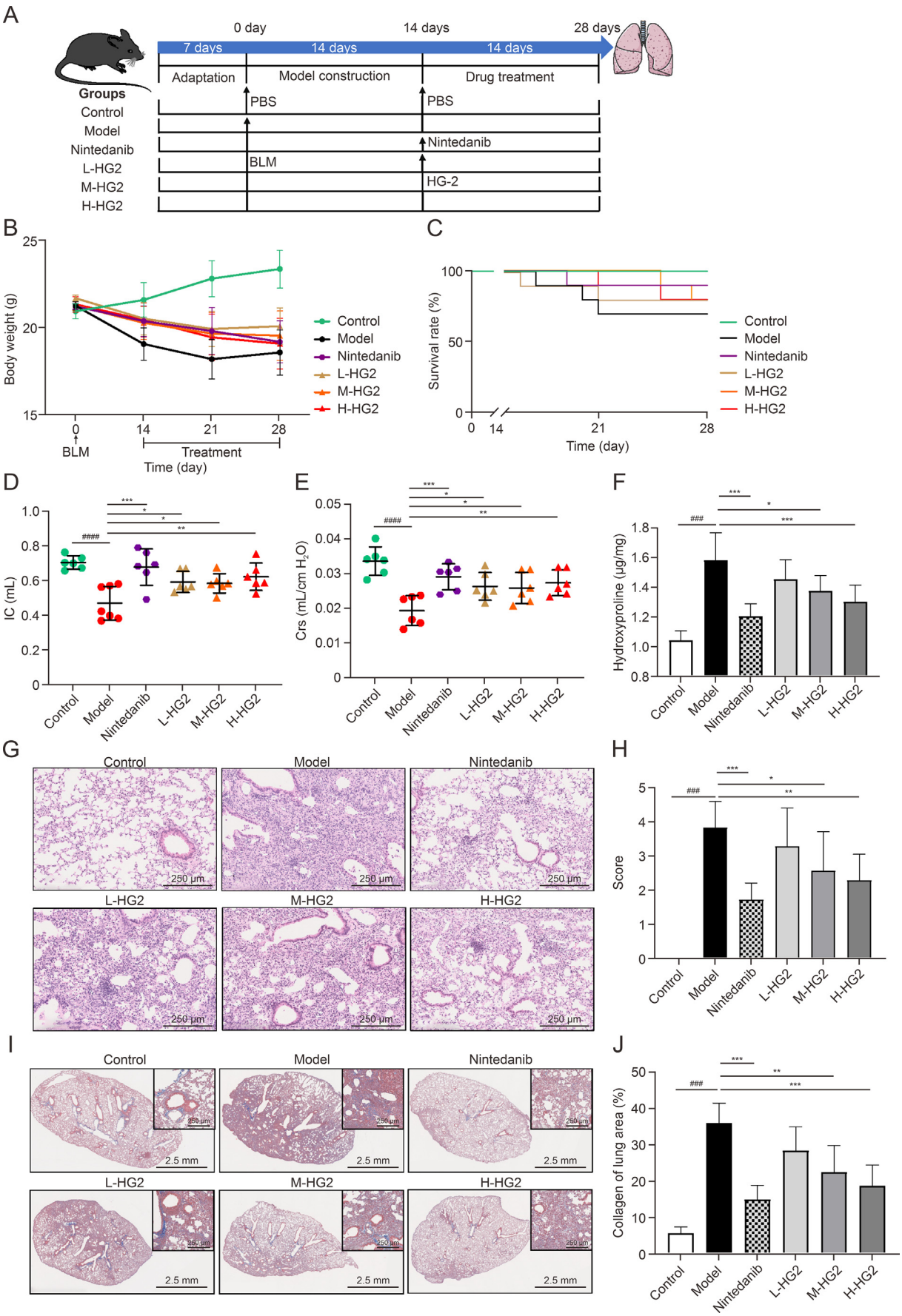
A
0 day
14 days
28 days
7 days
14 days
14 days
Adaptation
Model construction
Drug treatment
Groups
Control
Model
Nintedanib
L-HG2
M-HG2
H-HG2
PBS
PBS
Nintedanib
BLM
HG-2
B
Body weight (g)
Time (day)
BLM
Treatment
C
Survival rate (%)
Time (day)
D
IC (mL)
E
Crs (mL/cm H2O)
F
Hydroxyproline (μg/mg)
G
250 μm
H
Score
I
2.5 mm
J
Collagen of lung area (%)

group decreased. HG-2 and nintedanib could significantly improve the lung function of mice. In addition, HG-3 and HG-4 tended to upregulate Crs, but no significant difference was observed (Figs. 1D and E).

Hydroxyproline is a unique amino acid found in collagen tissue. Collagen deposition in mouse lung tissue was characterized by the quantitative detection of hydroxyproline content in lung tissue and Masson staining. Hydroxyproline content was significantly increased in the lung tissues of mice in the BLM group ($P < 0.001$), and a large number of proliferating blue collagen fibers were observed around the bronchial walls, small blood vessels, alveolar walls, and alveolar septa. The collagen content of the HG-4 group was lower than that of the BLM group, but there was no significant difference. The HG-2 group showed an improvement close to that observed in the nintedanib group; collagen content and hydroxyproline content were significantly reduced (Figs. 1F–H).

Another manifestation of PF is the massive proliferation and activation of fibroblasts into myofibroblasts, which mainly express α-SMA. The expression of α-SMA in lung tissue was detected based on immunohistochemistry analysis. α-SMA was mainly expressed around the bronchial wall and blood vessel wall in the control group. However, it significantly increased and was expressed in the alveolar wall and alveolar-interstitial region in the model group, thus, indicating that fibroblasts proliferated and were activated. The expression of α-SMA in the nintedanib and HG-2 groups decreased in the alveolar-interstitial region and was mainly expressed in the area around the bronchial wall. The source was bronchial smooth muscle cells. Compared to the model group, the expression of α-SMA in the HG-3 and HG-4 groups decreased, but no significant difference was observed (Figs. 1I and J). The above results showed that HG-2 showed a better effect on improving BLM-induced PF than other extracts and exhibited similar efficacy to nintedanib, and is worthy of further research into its composition and mechanism of action.

3.2. HG-2 dose-dependently improves BLM-induced PF in mice

Furthermore, low, medium, and high doses of HG-2 (50, 100, and 200 mg/kg) were administered to evaluate the improvement effects on PF (Fig. 2A). After the PF model was established, the weight of mice in the model group decreased significantly, and the weight of the mice in administration group tended to recover in a dose-dependent manner. Compared to the model group, the survival rate of HG-2 group also increased (Figs. 2B and C). Pulmonary function indicators showed that IC and Crs were significantly decreased in the model group ($P < 0.0001$), and nintedanib had a better effect on improving lung function ($P < 0.001$). Notably, all dose of HG-2 significantly increased the IC and Crs in mice (Figs. 2D and E). Furthermore, HG-2 reduced hydroxyproline content in fibrotic tissues in a dose-dependent manner (Fig. 2F). HE staining to assess the histopathologic changes in the lungs showed that the control mice had standard histology, while the model group showed collagen deposition and structural deformation. HG-2 improved the pathological degree of lung fibrosis (Figs. 2G and H). Masson staining was used to characterize the distribution of collagen fibers, and the corresponding results showed that HG-2 improved collagen deposition in BLM-induced PF (Figs. 2I and J).

3.3. HG-2 plays an anti-PF role by inhibiting the TGF-β1/Smad pathway

TGF-β is considered as a key driver of PF and its overactivation can induce fibroblasts to increase the production of pro-fibrotic factors such as collagen, fibronectin, and α-SMA [22]. The TGF-β1/Smad signaling pathway is considered as the classic pathway mediating the formation of PF [23]. TGF-β acts on the TGF-beta receptor type II (TGF-βRII) to recruit TGF-βRI, and activated TGF-βRI will phosphorylate Smad2 and Smad3 to form a complex with Smad4. The complex is then translocated to the nucleus to regulate the transcription and expression of fibrosis-related proteins [24].

The expression of TGF-β1 in mouse lung tissue was detected by ELISA. The levels of phosphorylation of Smad2/3 and expression of its downstream proteins including α-SMA and COL1A1 were detected by Western blotting. ELISA results showed that the level of TGF-β1 in the lung tissue of mice in the model group was significantly increased. However, HG-2 and nintedanib treatment attenuated TGF-β1 expression compared to the model group (Fig. 3A). The Western blotting results showed that the phosphorylation level of Smad2/3 and the protein expression levels of α-SMA and COL1A1 in the model group were significantly increased. Each dosage group of HG-2 significantly reduced the levels of phosphorylated Smad 2/3, and the high-dose HG-2 group had the similar inhibitory effect on the expression of α-SMA and COL1A1 as nintedanib (Figs. 3B–E).

3.4. The main components of HG-2 were identified by UHPLC-QTOF-MS/MS

The high-resolution MS data were compared to the known components of the HG extract, and the MS/MS data were collected under different collision voltages. Twenty-six components in HG-2 were identified, including 20 anthraquinones, 4 iridoids, and 2 anthraquinone glycosides. Some of the compounds were isomers. The basic information of each identified ingredient is shown in Table 1, and the structural formula is summarized in Fig. S1. The total ion chromatogram (TIC) and extracted ion chromatogram (EIC) of compounds at high levels are shown in Figs. 4A and B. The peak area of the top 10 compounds in HG-2 are shown in Fig. 4C, all of which are anthraquinones. The levels of rubiadin 1-methyl ether and rubiadin were higher than those of other components.

3.5. The multi-target regulatory effect of HG-2 on PF was revealed by network pharmacology

Drug target prediction and PF disease-related targets were identified based on the 26 components in HG-2 identified by UHPLC-QTOF-MS/MS. A total of 429 HG-2-related gene targets and 586 PF-related gene targets were collected, and 35 common genes were identified as potential HG-2 targets for PF treatment. The network of “drug-ingredient-target-disease” was constructed based on intersecting targets. Nodes with different colors and shapes represented drugs, components, targets, and diseases. The edges were used to connect the associations between components, core targets, and diseases to characterize the complex regulatory network of multiple HG-2 components on PF. According to the degree of drug-target interaction and the content of the compound

Fig. 2. Effects of different doses of *Prismatomeris connata* Y. Z. Ruan (Huang Gen, HG) ethyl acetate extract (HG-2) on pulmonary fibrosis (PF) in mice. (A) Schematic diagram of animal model construction and HG-2 administration program schedule. (B, C) Body weight (B) and survival rate (C) of mice treated with bleomycin (BLM) and HG-2. (D, E) Inspiratory capacity (IC) (D) and compliance (Crs) (E) were detected by FlexiVent to evaluate the fibrotic changes in lungs. (F) Quantitative detection of hydroxyproline in right lung tissue. (G, H) Representative images of hematoxylin and eosin staining in lung tissue (G) and histopathology scores (H) from 0 to 5 based on the fibrotic area. (I, J) Representative images of Masson staining in lung tissue (I) (inset: random field of view) and the percentage of collagen of lung area (J). All data are expressed as the mean ± standard deviation (SD) ($n = 6$ per group). $^{###}P < 0.001$ and $^{####}P < 0.0001$, compared to the control group; $^{*}P < 0.05$, $^{**}P < 0.01$, and $^{***}P < 0.001$, compared to the model group. L: low dose; M: medium dose; H: high dose; PBS: phosphate-buffered saline.

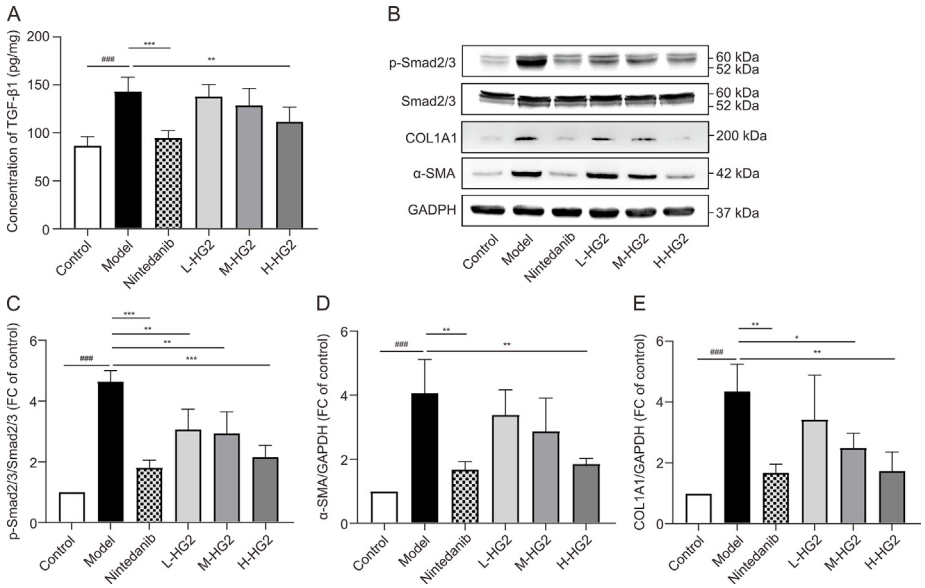

Fig. 3. *Prismatomeris connata* Y. Z. Ruan (Huang Gen, HG) ethyl acetate extract (HG-2) inhibited the transforming growth factor beta 1(TGF-β1)/suppressor of mothers against decapentaplegic (Smad) pathway in bleomycin (BLM)-induced pulmonary fibrosis (PF) in mice. (A) TGF-β1 levels were determined by enzyme-linked immunosorbent assay (ELISA) in the homogenized protein from the right lung. (B) Protein expression of p-Smad2/3, Smad2/3, collagen type I alpha 1 chain (COL1A1), α-smooth muscle actin (α-SMA), and glyceraldehyde 3-phosphate dehydrogenase (GAPDH) examined by Western blotting. (C–E) The ratios of p-Smad2/3 to total Smad2/3 (C), α-SMA to GAPDH (D), and COL1A1 to GAPDH (E) are presented as fold changes (FCs) relative to the control group. Protein expression levels were normalized using GAPDH and presented as a fold changed relative to the control group. Values are the mean ± standard deviation (SD) of three separate experiments. $^{###}P < 0.001$, compared to the control group; $^{*}P < 0.05$, $^{**}P < 0.01$, and $^{***}P < 0.001$, compared to the model group. L: low dose; M: medium dose; H: high dose.

Table 1
Twenty-six components in *Prismatomeris connata* Y. Z. Ruan (Huang Gen, HG) ethyl acetate extract (HG-2) were identified by liquid chromatography-mass spectrometry (LC-MS).

No.	Compound name	Type	Molecular formula	Retention time (min)	Peak area (mAU• min)
1	Scopoletin	Anthraquinone	$C_{10}H_8O_4$	2.01	396,915
2	2-Methylanthraquinone	Anthraquinone	$C_{15}H_{10}O_2$	1.97	323,909
3	1-Hydroxy-2-methylanthraquinone	Anthraquinone	$C_{15}H_{10}O_3$	14.41	4,973,898
4	Rubiadin	Anthraquinone	$C_{15}H_{10}O_4$	16.31	30,879,131
5	2-Hydroxy-3-methoxy-9,10-anthraquinone	Anthraquinone	$C_{15}H_{10}O_4$	9.34	9,361,089
6	Nordamnacanthal	Anthraquinone	$C_{15}H_8O_5$	8.44	4,686,412
7	Damnacanthal	Anthraquinone	$C_{16}H_{10}O_5$	12.74	4,024,395
8	Rubiadin 1-methyl ether	Anthraquinone	$C_{16}H_{12}O_4$	13.41	32,637,910
9	2-(Methoxymethyl)-1,3-dihydroxyanthraquinone	Anthraquinone	$C_{16}H_{12}O_5$	9.06	8,933,528
10	2-(Ethoxymethyl)-1,3-dihydroxy-9,10-anthraquinone	Anthraquinone	$C_{17}H_{14}O_5$	13.06	2,807,415
11	1-Hydroxy-2,3-dimethoxy-7-methylanthraquinone	Anthraquinone	$C_{17}H_{14}O_5$	14.05	892,266
12	7-Hydroxy-1,2-dimethoxy-6-methylanthraquinone	Anthraquinone	$C_{17}H_{14}O_5$	15.75	295,422
13	1,3,8-Trihydroxy-7-methoxy-2-methylanthraquinone	Anthraquinone	$C_{16}H_{12}O_6$	15.83	2,067,238
14	3-Hydroxy-5,6-dimethoxy-2-methyl-1,2,3,4-tetrahydroanthraquinone	Anthraquinone	$C_{17}H_{18}O_5$	11.35	29,342
15	1,3-Dihydroxy-5,6-dimethoxy-2-methylanthraquinone	Anthraquinone	$C_{17}H_{14}O_6$	15.20	10,904,816
16	1,3-Dihydroxy-6-methoxy-2-(methoxymethyl)-9,10-anthraquinone	Anthraquinone	$C_{17}H_{14}O_6$	15.73	2,948,454
17	2-Hydroxy-4,6,7-trimethoxy-3-methylanthraquinone	Anthraquinone	$C_{18}H_{16}O_6$	14.10	934,472
18	3-Hydroxy-1,5,6-trimethoxy-2-methylanthraquinone	Anthraquinone	$C_{18}H_{16}O_6$	12.32	8,339,566
19	1,3-Dihydroxy-5,6-dimethoxy-2-methoxy-methylanthraquinone	Anthraquinone	$C_{18}H_{16}O_7$	9.57	730,664
20	4-Hydroxy-1,2,3-trimethoxy-7-hydroxymethylanthraquinone	Anthraquinone	$C_{18}H_{16}O_7$	16.05	796,762
21	Prismatomerin	Iridoid	$C_{20}H_{16}O_7$	17.36	93,011
22	Deacetyl asperuloside	Iridoid	$C_{16}H_{20}O_{10}$	0.92	33,154
23	Deacetyl asperulosidic acid	Iridoid	$C_{16}H_{22}O_{11}$	0.80	46,290
24	Asperulosidic acid	Iridoid	$C_{18}H_{24}O_{12}$	0.84	487,361
25	Damnacanthol 3-*O*-β-primeveroside	Anthraquinone glycoside	$C_{27}H_{30}O_{14}$	15.32	10,581
26	Rubiadin 3-*O*-β-primerveroside	Anthraquinone glycoside	$C_{26}H_{28}O_{13}$	9.73	151,758

in the extract, the eight vital active components were screened, including scopoletin (D1), 1-hydroxy-2-methylanthraquinone (D3), rubiadin (D4), damnacanthal (D7), rubiadin 1-methyl ether (D8), 7-hydroxy-1,2-dimethoxy-6-methylanthraquinone (D12), 3-hydroxy-1,5,6-trimethoxy-2-methylanthraquinone (D18), and 4-hydroxy-1,2,3-trimethoxy-7-hydroxymethylanthraquinone (D20) (Fig. 5A).

The PPI network was used to visualize the interaction between targets. The main target categories based on degree value included receptor tyrosine kinases (epidermal growth factor receptor (EGFR), erb-b2 receptor tyrosine kinase 2 (ERBB2), PDGFRA, PDGFRB, and c-ros oncogene 1 receptor tyrosine kinase (ROS1)), metalloproteinases (MMP1, MMP2, MMP7, and MMP9), protein kinases (MAPK1 and Janus kinase 2 (JAK2)), inflammation and oxidation related enzymes (PTGS2 and nitric oxide synthase 2 (NOS2)), andother categories (JUN, STAT3, cyclin D1 (CCND1), and phosphatidylinositol-4,5-bisphosphate 3-kinase catalytic subunit alpha (PIK3CA)) (Fig. 5B). Then all intersection genes were used

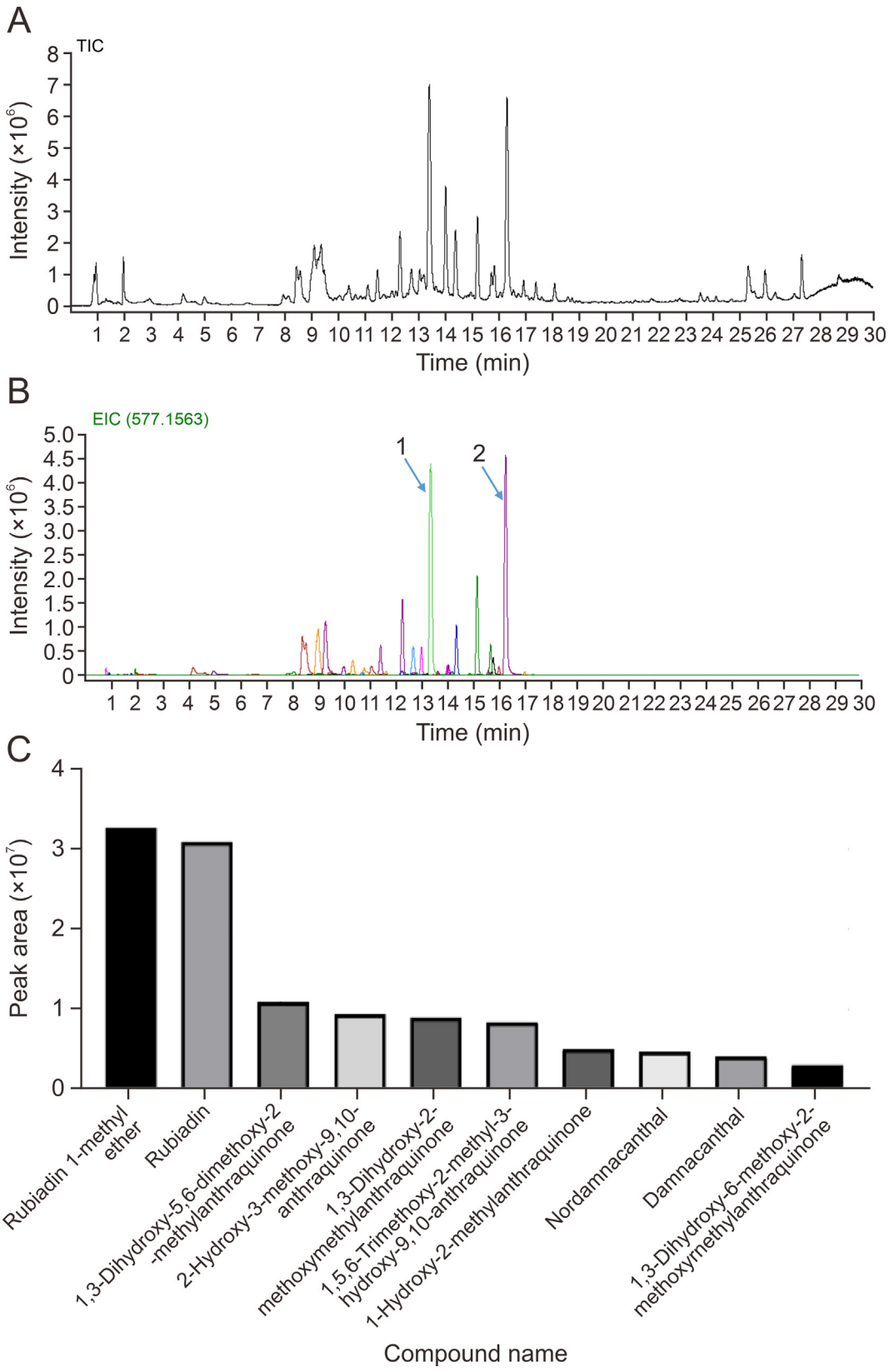

Fig. 4. Determination of bioactive compounds in *Prismatomeris connata* Y. Z. Ruan (Huang Gen, HG) ethyl acetate extract (HG-2) by ultra-high-performance liquid chromatography coupled with quadrupole time-of-flight tandem mass spectrometry (UHPLC-QTOF-MS/MS). (A) The total ion chromatogram (TIC) of HG-2. (B) The extracted ion chromatogram (EIC) of rubiadin 1-methyl ether (1) and rubiadin (2). (C) Peak area of the main components of HG-2.

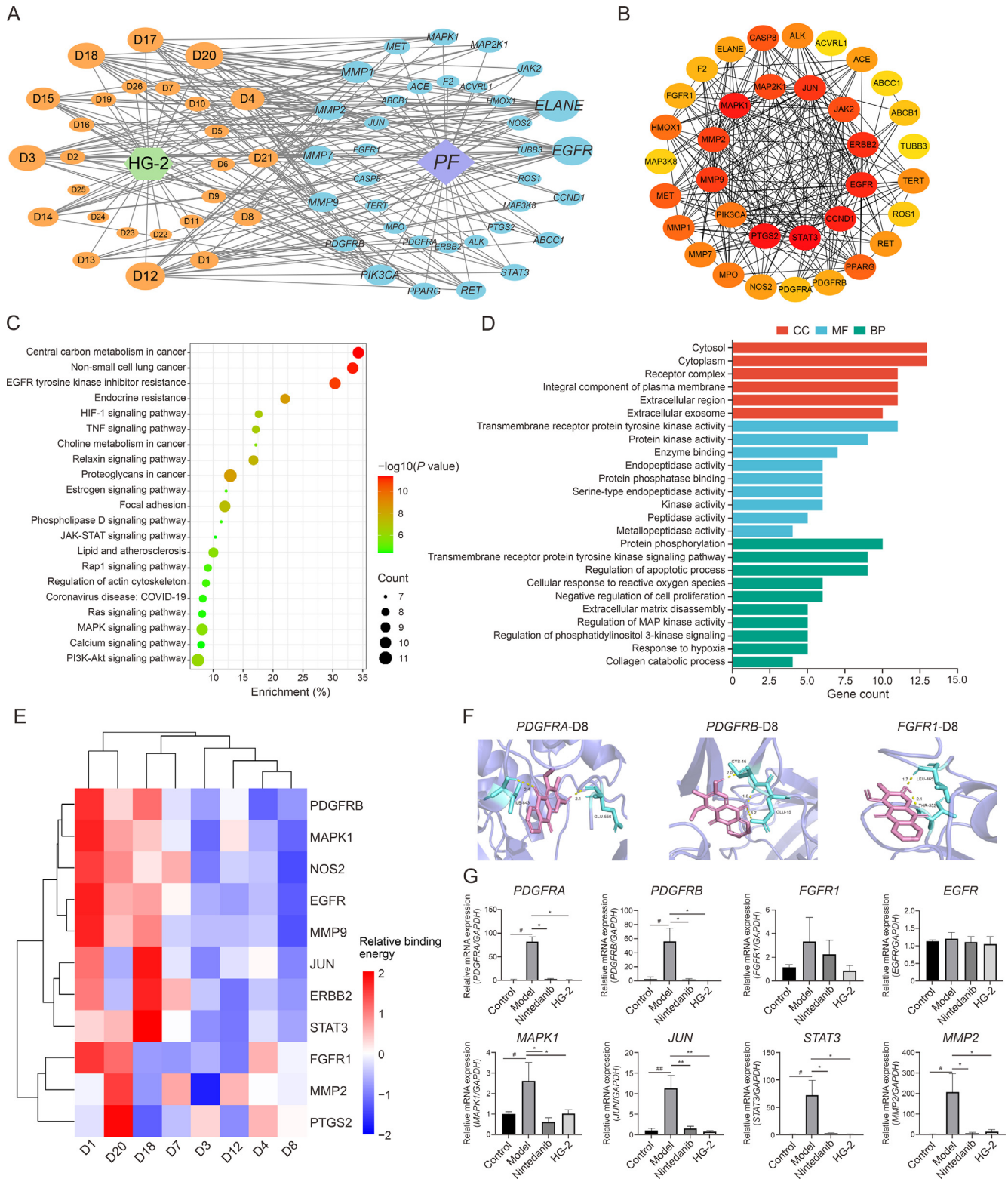

Fig. 5. Network pharmacological analysis and validation of related targets. (A) The "drug-components-target-disease" network of *Prismatomeris connata* Y. Z. Ruan (Huang Gen, HG) ethyl acetate extract (HG-2). Nodes are colored to distinguish object attributes, with green representing drugs, orange representing components, purple representing diseases, and blue representing genes. The size of nodes represents the correlation between components and targets; the larger the node, the higher the correlation. D1: scopoletin; D2: 2-methylanthraquinone; D3: 1-hydroxy-2-methylanthraquinone; D4: rubiadin; D5: 2-hydroxy-3-methoxy-9,10-anthraquinone; D6: nordamnacanthal; D7: damnacanthal; D8: rubiadin 1-methyl ether; D9: 2-(methoxymethyl)-1,3-dihydroxyanthraquinone; D10: 2-(ethoxymethyl)-1,3-dihydroxy-9,10-anthraquinone; D11: 1-hydroxy-2,3-dimethoxy-7-methylanthraquinone; D12: 7-hydroxy-1,2-dimethoxy-6-methylanthraquinone; D13: 1,3,8-trihydroxy-7-methoxy-2-methylanthraquinone; D14: 3-hydroxy-5,6-dimethoxy-2-methyl-1,2,3,4-tetrahydroanthraquinone; D15: 1,3-dihydroxy-5,6-dimethoxy-2-methylanthraquinone; D16: 1,3-dihydroxy-6-methoxy-2-(methoxymethyl)-9,10-anthraquinone; D17: 2-hydroxy-4,6,7-trimethoxy-3-methylanthraquinone; D18: 3-hydroxy-1,5,6-trimethoxy-2-methylanthraquinone; D19: 1,3-dihydroxy-5,6-dimethoxy-2-methoxy-methylanthraquinone; D20: 4-hydroxy-1,2,3-trimethoxy-7-hydroxymethylanthraquinone; D21: prismatomerin; D22: deacetyl asperuloside; D23: deacetyl asperulosidic acid; D24: asperulosidic acid; D25: damnacanthol 3-*O*-β-primeveroside; D26: rubiadin 3-*O*-β-primerveroside. (B) The protein-protein interaction (PPI) network of targets associated with HG-2

for GO enrichment analysis and KEGG pathway enrichment analysis. KEGG enrichment showed that common pathways involved in PF included the hypoxia-inducible factor 1 (HIF-1) signaling pathway, tumor necrosis factor (TNF) signaling pathway, JAK-STAT signaling pathway, reliability, availability and serviceability (RAS) signaling pathway, and MAPK signaling pathway (Fig. 5C). GO enrichment included molecular function (MF), cellular component (CC), and biological process (BP), which involved a wide range of physiological activities, including protein phosphorylation, regulation of transmembrane receptor protein tyrosine kinases, cellular responses to reactive oxygen species, negative regulation of cell proliferation,regulation of apoptotic process, and ECM disassembly (Fig. 5D).

Molecular docking was used to evaluate the interaction between the drug component and the target protein. When the binding energy was less than 0 kJ/mol, the ligand and the receptor were considered to be free to combine, while a binding energy ≤ -5 kJ/mol was considered to have favorable affinity. We found that the eight key active components showed a favorable affinity to the vital target proteins (Table S2). In particular, rubiadin 1-methyl ether (D8) and rubiadin (D4) were present in HG-2 at higher levels than the other compounds. They also exhibited strong binding to the core target (Fig. 5E), which might be the critical pharmacological effect of HG-2 in treating PF. Then, the core component rubiadin 1-methyl ether (D8), as well as the tyrosine kinase receptors, PDGFR and FGFR, were used as examples for molecular docking studies to visualize binding conformations (Fig. 5F). Considering the significant therapeutic effect of multiple tyrosine kinase inhibitors in PF, we verified the expression of PF-related genes in mouse lung samples by qPCR. Notably, the results showed that HG-2 had multiple tyrosine kinase inhibitory activities that had comparable inhibitory effects to nintedanib on *PDGFRA*, *PDGFRB*, and *FGFR1*, and better inhibitory effects on *MAPK1*, *JUN*, and *STAT3*, and *MMP2* (Fig. 5G).

3.6. HG-2 reverts the metabolic profile of mice with BLM-induced PF

As shown in Fig. 6A, MSI presented the *in situ* spatial distribution of metabolites and comprehensively and accurately described their changes in the metabolic levels in the lung tissues of mice after BLM modeling and high-dose HG-2 intervention (Fig. 6A). Taking the positive ion acquisition mode as an example, AFADESI-MSI can obtain high quality images even in high and low abundances (Fig. 6B). To further analyze the changes of the metabolic profile in BLM-induced PF, an orthogonal partial least squares discriminant analysis (OPLS-DA) model was constructed and verified, showing that the model was robust without overfitting and had good predictive ability. Both groups exhibited obvious clustering and grouping tendencies in positive and negative ion modes (Fig. 6C). After differential metabolite screening, principal component analysis (PCA) and heat map analysis were used to assess screening reliability and characterize differential metabolic profiles. PCA scores showed that the model group and the control group could be clearly distinguished, indicating that there was a significant difference in the metabolic profile of differential metabolites in the model group. The projections of the HG-2 group and the control group partially overlapped, indicating that HG-2 had a certain improvement effect on differential metabolites (Fig. 6D). The abundance differences in metabolism were visualized using heat maps, further elucidating the significant regulatory effect of HG-2 on BLM-induced metabolic disorders in mice (Fig. 6E).

3.7. MSI characterizes the heterogeneous distribution of metabolites in lung tissue and BLM-induced metabolic reprogramming in PF

Metabolic reprogramming has become an essential event in the pathogenesis of PF, and metabolic disorders of carbohydrates, lipids, and proteins have been demonstrated [10,25,26]. After the identification of differential metabolites, it was found that the metabolic changes of BLM-induced PF in mice involved amino acids, including the upregulation of arginine, proline, glutamic acid, FAs, the upregulation of FAs (FA 16:3 and FA 18:1) and phospholipids, and the downregulation of phosphatidylcholine (PC) 32:0, PC 34:2, and phosphatidylserine (PS) 36:2 (Table S3). The abundance trends of PF biomarkers such as proline, hypoxanthine, arginine, and glutamine in this study were consistent with those reported in previous studies [9,10].

Metabolites in lung tissue can be mainly characterized using three distribution characteristics. Among them, some metabolites are highly enriched specifically around the bronchi, including amino acids, tricarboxylic acid cycle (TCA) cycle intermediates, special phospholipids, such as creatine, fumarate, succinate, citrate, adenosine diphosphate (ADP), and phosphatidic acid (PA) 46:0. Some metabolites are evenly distributed in the lung parenchyma, such as phosphoserine glycerophosphoethanolamine, PC 32:0, and PS 36:2. Other metabolites are highly enriched at the edge of lung structure, including spermine, spermidine, carnitine and acyl-carnitines, FAs (FA 18:1 and FA 20:4), and monoglycerol (MG) FA esters (MG 16:0, MG 16:1, and MG 18:1) (Figs. 7A and S2–S4). Differential metabolite pathway analyses revealed that the metabolic dysregulation of BLM-induced lung fibrosis in mice involved multiple pathways, including alanine, aspartate and glutamate metabolism, arginine biosynthesis, glycerophospholipid metabolism, arginine and proline metabolism, TCA cycle, and purine metabolism (Fig. 7B).

The metabolic network was constructed further to clarify the role of differential metabolites in PF. We found that the heterogenous distribution of metabolites in lung tissue was closely related to the type of metabolite and the biochemical processes. After BLM modeling, the abundance and distribution characteristics of

treatment of pulmonary fibrosis (PF). The darker red hue of the node indicates that the gene plays an important role in the network. (C) Kyoto Encyclopedia of Genes and Genomes (KEGG) enrichment analysis. (D) Gene Ontology (GO) enrichment analysis of gene targets, including molecular function (MF), cellular component (CC), and biological process (BP). (E) Heat map of molecular docking binding energies between key components and core targets. (F) Molecular docking conformation and binding sites of platelet-derived growth factor receptor alpha (*PDGFRA*)-D8, *PDGFRB*-D8, and fibroblast growth factor receptor 1 (*FGFR1*)-D8. (G) Quantitative polymerase chain reaction (qPCR) analysis of the messenger RNA (mRNA) levels of *PDGFRA*, *PDGFRB*, *FGFR1*, epidermal growth factor receptor (*EGFR*), mitogen-activated protein kinase 1 (*MAPK1*), Jun proto-oncogene (*JUN*), signal transducer and activator of transcription 3 (*STAT3*), and matrix metalloproteinase 2 (*MMP2*) in lung tissue. The data are expressed as the mean ± standard deviation (SD). $^{\#}P < 0.05$ and $^{\#\#}P < 0.01$, compared to the control group; $^{*}P < 0.05$ and $^{**}P < 0.01$, compared to the model group. MAP3K8: MAPK kinase kinase 8; HMOX1: heme oxygenase 1; FGFR1: fibroblast growth factor receptor 1; F2: coagulation factor II; ELANE: neutrophil elastase; CASP8: caspase 8; ALK: anaplastic lymphoma kinase; ACVRL1: activin A receptor like type 1; ACE: angiotensin I converting enzyme; ABCC1: adenosine triphosphate (ATP) binding cassette subfamily C member 1; ABCB1: ATP binding cassette subfamily B member 1; TUBB3: tubulin beta 3 class III; TERT: telomerase reverse transcriptase; ROS1: c-ros oncogene 1 receptor tyrosine kinase; RET: ret proto-oncogene; PPARG: peroxisome proliferator activated receptor gamma; NOS2: nitric oxide synthase 2; MPO: myeloperoxidase; MET: *MET* proto-oncogene receptor tyrosine kinase; MAPK1: mitogen-activated protein kinase 1; JAK2: Janus kinase 2; ERBB2: erb-b2 receptor tyrosine kinase 2; CCND1: cyclin D1; PTGS2: prostaglandin-endoperoxide synthase 2; PI3KCA: phosphatidylinositol-4,5-bisphosphate 3-kinase catalytic subunit alpha; HIF-1: hypoxia-inducible factor 1; TNF: tumor necrosis factor; JAK: Janus kinase; Rap1: Ras-association proximate 1; COVID-19: coronavirus disease 2019; MAPK: mitogen-activated protein kinase; PI3K-Akt: phosphoinositide 3 kinase-protein kinase B; MAP: mitogen-activated protein; GAPDH: glyceraldehyde 3-phosphate dehydrogenase.

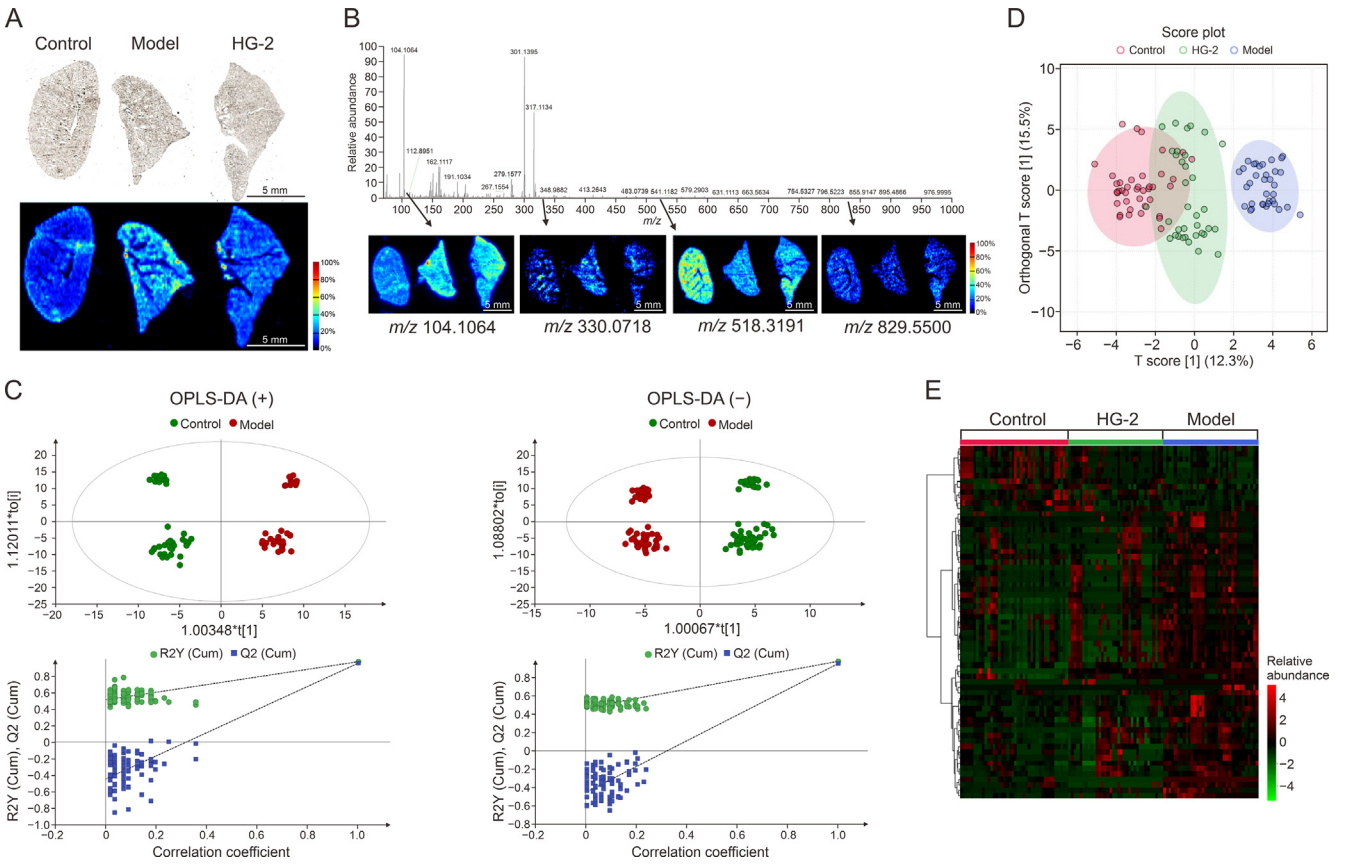

Fig. 6. Mass spectrometry (MS) data analysis. (A) Optical image and mass spectrometry image (MSI) showing the structural profiles of lung tissue. (B) Total ion flow and mass spectra of lung tissue collected under positive ion mode. (C) The orthogonal partial least squares discriminant analysis (OPLS-DA) score plots and permutations test in positive and negative ion modes. (D) The principal component analysis score plots of different metabolites in each group. (E) Heat maps showing the abundance of differential metabolites in each group. HG-2: *Prismatomeris connata* Y. Z. Ruan (Huang Gen, HG) ethyl acetate extract. Cum: cumulative.

metabolites changed. Metabolites closely related to energy metabolism, such as creatine, fumarate, succinate, citrate, and adenosine triphosphate (ATP), were enriched around the bronchus, while their abundances decreased significantly after fibrosis. Carnitine, acyl-carnitine, FA, and the downstream metabolites, MG FA esters, were highly enriched at the edge of lung tissue and significantly upregulated following fibrosis. Purine-related metabolites were widely distributed in the lung parenchyma and significantly upregulated after fibrosis. Phospholipid metabolites were an essential part of the alveoli and are widely distributed in the lungs, which were also significantly disordered after fibrosis (Fig. 7C).

3.8. MSI visualizes the metabolic regulation of HG-2 in PF

The regulatory effects of HG-2 on differential metabolites are summarized in Table 2. Common amino acids (valine, aspartic acid, threonine, and citrulline), FAs (FA 14:0 and FA 16:2), acylcarnitines (acetylcarnitine and propionylcarnitine), and MGs (MG 18:1 and MG 22:6) were significantly upregulated in the lungs of mice with BLM-induced PF and were significantly downregulated following HG-2 administration. However, the abundance of glycerophospholipids and phospholipids, including glycerophosphorylcholine, glyceraldehyde-3-phosphate, cholesterol sulfate, and PS 36:2, was significantly downregulated after BLM modeling and significantly upregulated following HG-2 administration (Fig. 8A). After pathway enrichment analysis, it was found that HG-2 could improve metabolic disorders by regulating arginine biosynthesis, alanine, aspartate and glutamate metabolism, glycerophospholipid metabolism, and arachidonic acid metabolism pathways (Figs. 8B and C).

4. Discussion

Fibrosis is the ultimate pathological feature of many standard chronic inflammatory processes. Currently, only nintedanib and pirfenidone are used to treat IPF. The development of new drugs for various targets of PF disease is in full swing. According to the mechanism of action, the development of new drugs for IPF can be divided into three categories, including targeting protein kinase-related signaling pathways such as tyrosine kinases [27–29] and Src family kinases [30], targeting G protein-coupled receptors such as sphingosine-1-phosphate receptors [31,32] and autotaxin-lysophosphatidic acid axis [33–35], as well as targeting other fibrotic mediators such as transcription factors, nuclear receptors, and integrins [36,37]. Unfortunately, most drugs were abandoned after clinical trials due to lack of benefit or toxicity. Given the interaction of multiple pathological mechanisms in PF, single-target therapeutic drugs are unlikely to control the progression of the disease. In this study, we initially reported a natural source of HG ethyl acetate extract (HG-2) has a significant therapeutic effect on PF. Further, we explored its overall regulatory network mechanism based on network pharmacology and spatially resolved metabolomics.

First, a BLM-induced PF mouse model was used to evaluate the therapeutic effect of HG extracts (HG-2, HG-3, and HG-4). HG-2

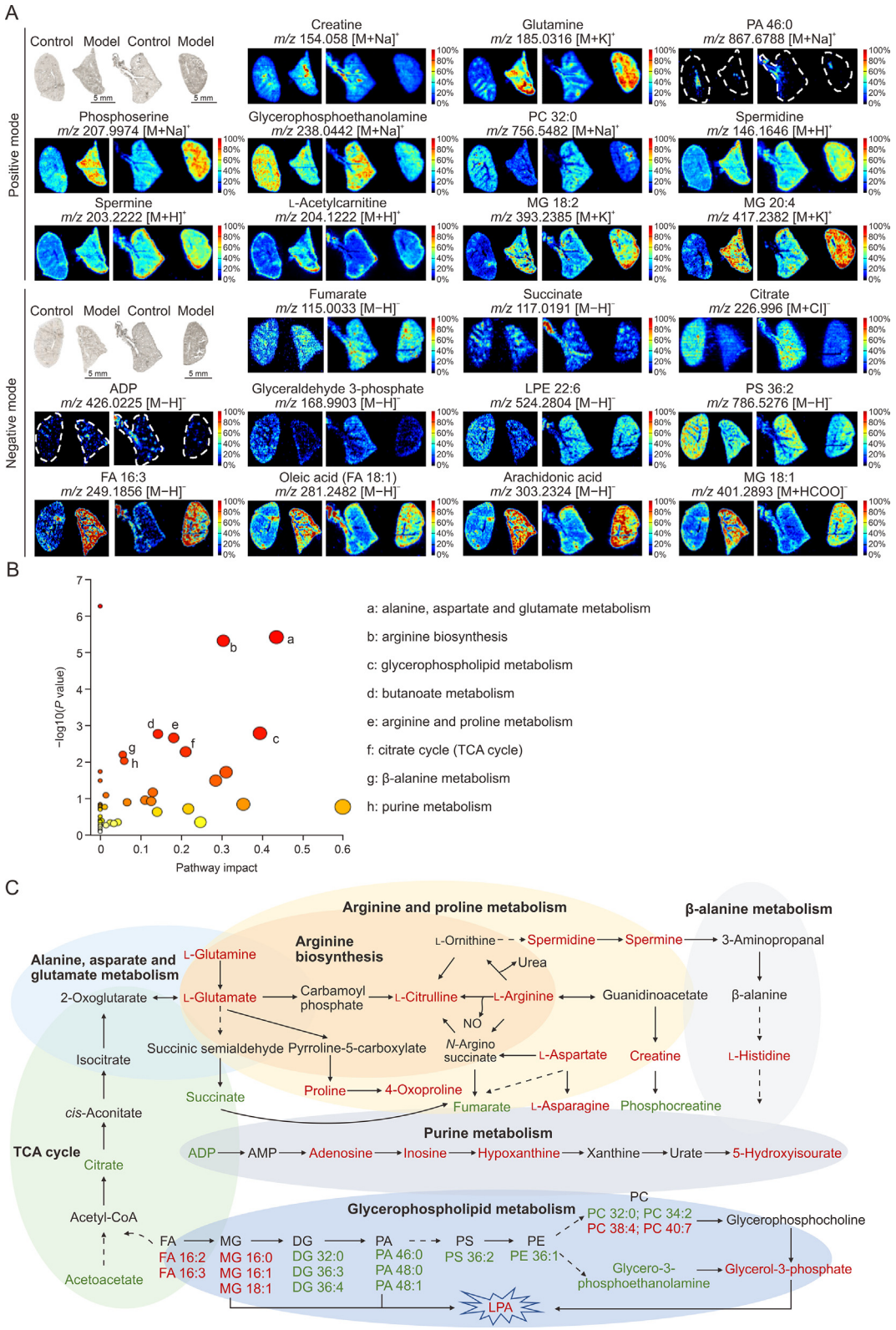

Fig. 7. Visualization of differential metabolites and pathway enrichment analyses of bleomycin (BLM)-induced pulmonary fibrosis (PF) in mice. (A) A representative mass spectrometry image (MSI) of differential metabolites in positive and negative ion modes. The consistency of metabolite distribution within the group was shown by the left and right slices. (B) Pathway enrichment analysis of differential metabolites from the Kyoto Encyclopedia of Genes and Genomes (KEGG) database. (C) The construction of metabolic networks indicating the function and changes of differential metabolites in pathways. Metabolites in green indicate a reduction in abundance, while those in red indicate an increase in abundance. PA: phosphatidic acid; PC: phosphatidylcholine; MG: monoglyceride; ADP: adenosine diphosphate; LPE: lyso-phosphatidylethanolamine; PS: phosphatidylserine; FA: fatty acid; TCA: tricarboxylic acid; NO: nitric oxide; AMP: adenosine monophosphate; DG: diacylglycerol; PE: phosphatidylethanolamine.

Table 2
The metabolites of pulmonary fibrosis (PF) regulated by *Prismatomeris connata* Y. Z. Ruan (Huang Gen, HG) ethyl acetate extract (HG-2) as detected by ambient fluid desorption electrospray ionization-mass spectrometry imaging (AFADESI-MSI) in positive and negative ion modes.

Metabolite identification	Elemental composition	Adduct	Measured (*m/z*)	Error (ppm)[b]	FC (model/control)[c]	FC (HG-2/model)[d]
L-Valine[a]	$C_5H_{11}NO_2$	$[M-H]^-$	116.0714	−2.58	↑$^{###}$	↓[a]
Threonine[a]	$C_4H_9NO_3$	$[M-H]^-$	118.0503	−5.93	↑$^{####}$	↓***
Asparagine[a]	$C_4H_8N_2O_3$	$[M-H]^-$	131.0458	−3.05	↑$^{####}$	↓*
Aspartic acid[a]	$C_4H_7NO_4$	$[M-H]^-$	132.0299	−2.27	↑$^{#}$	↓**
Glutamine[a]	$C_5H_{10}N_2O_3$	$[M-H]^-$	145.0612	−4.83	↑$^{####}$	↓****
Glyceraldehyde-3-phosphate[a]	$C_3H_7O_6P$	$[M-H]^-$	168.9903	−2.37	↓$^{#}$	↑*
Glutamine[a]	$C_5H_{10}N_2O_3$	$[M+K]^+$	185.0316	−3.78	↑$^{###}$	↓**
p-Cresol sulfate[a]	$C_7H_8O_4S$	$[M-H]^-$	187.0066	−2.67	↑$^{##}$	↓**
8-Ocimenyl acetate	$C_{12}H_{18}O_2$	$[M-H]^-$	193.1227	−3.62	↑$^{####}$	↓****
Gluconic acid[a]	$C_6H_{12}O_7$	$[M-H]^-$	195.0505	−2.56	↑$^{#}$	↓****
Spermine[a]	$C_{10}H_{26}N_4$	$[M+H]^+$	203.2222	−3.94	↑$^{####}$	↓***
Acetylcarnitine[a]	$C_9H_{17}NO_4$	$[M+H]^+$	204.1222	−3.92	↑$^{####}$	↓****
5-Hydroxyisourate	$C_5H_4N_4O_4$	$[M+Na]^+$	207.0134	4.35	↑$^{####}$	↓*
Phosphoserine[a]	$C_3H_8NO_6P$	$[M+Na]^+$	207.9974	−3.37	↑$^{###}$	↓**
Citrulline	$C_6H_{13}N_3O_3$	$[M+K]^+$	214.0580	−3.74	↑$^{####}$	↓*
Propionylcarnitine[a]	$C_{10}H_{19}NO_4$	$[M+H]^+$	218.1377	−4.58	↑$^{###}$	↓**
FA 14:0[a]	$C_{14}H_{28}O_2$	$[M-H]^-$	227.2013	−1.76	↑$^{####}$	↓****
Glutamyl-taurine	$C_7H_{14}N_2O_6S$	$[M+H]^+$	255.0651	2.35	↑$^{####}$	↓****
Glycerophosphocholine[a]	$C_8H_{20}NO_6P$	$[M+Na]^+$	280.0910	−3.57	↓$^{##}$	↑*
FA 16:2	$C_{16}H_{28}O_2$	$[M+HCOO]^-$	297.2068	−1.01	↑$^{####}$	↓****
Arachidonic acid[a]	$C_{20}H_{32}O_2$	$[M-H]^-$	303.2324	−1.98	↑$^{####}$	↓*
Adenosine[a]	$C_{10}H_{13}N_5O_4$	$[M+HCOO]^-$	312.0938	−3.84	↑$^{####}$	↓*
Cytidine monophosphate[a]	$C_9H_{14}N_3O_8P$	$[M^-H]^-$	322.0437	−2.79	↑$^{##}$	↓****
15*H*-11,12-EETA[a]	$C_{20}H_{32}O_4$	$[M-H]^-$	335.2223	1.79	↑$^{##}$	↓****
13-HDoHE	$C_{22}H_{32}O_3$	$[M+Na]^+$	367.2225	−5.17	↑$^{####}$	↓*
Tetradecanoylcarnitine	$C_{21}H_{41}NO_4$	$[M+H]^+$	372.3091	−4.57	↑$^{####}$	↓****
MG 18:3	$C_{21}H_{36}O$	$[M+K]^+$	391.2226	−4.86	↑$^{####}$	↓*
Hexadecenoylcarnitine	$C_{23}H_{43}NO_4$	$[M+H]^+$	398.3248	−4.27	↑$^{###}$	↓*
Palmitoylcarnitine[a]	$C_{23}H_{45}NO_4$	$[M+H]^+$	400.3404	−4.25	↑$^{##}$	↓*
MG 18:1	$C_{21}H_{40}O_4$	$[M+HCOO]^-$	401.2893	−3.99	↑$^{####}$	↓***
MG 20:4	$C_{23}H_{38}O_4$	$[M+K]^+$	417.2382	−4.79	↑$^{####}$	↓*
Linoleylcarnitine[a]	$C_{25}H_{45}NO_4$	$[M+H]^+$	424.3403	−4.24	↑$^{####}$	↓*
MG 22:6	$C_{25}H_{38}O_4$	$[M+HCOO]^-$	447.2736	−3.58	↑$^{###}$	↓*
Cholesterol sulfate[a]	$C_{27}H_{46}O_4S$	$[M-H]^-$	465.3025	−4.08	↓$^{####}$	↑*
PC 32:0[a]	$C_{40}H_{80}NO_8$	$[M+Na]^+$	756.5482	−4.23	↓$^{#}$	↑**
PE 36:1[a]	$C_{41}H_{80}NO_8P$	$[M+Na]^+$	768.5516	0.26	↓$^{#}$	↑***
PC 34:2[a]	$C_{42}H_{80}NO_8P$	$[M+Na]^+$	780.5475	−5.00	↓$^{##}$	↑**
PS 36:2	$C_{42}H_{78}NO_{10}P$	$[M-H]^-$	786.5276	−1.91	↓$^{####}$	↑***

[a] Metabolites with exact tandem mass spectrometry (MS/MS) data were identified in the databases.
[b] Error (ppm) = ((Measured *m/z* − theoretical *m/z*)/theoretical *m/z*) × 10^6.
[c] The ratio of peak intensity between the model group and the control group. $^{#}P < 0.05$, $^{##}P < 0.01$, $^{###}P < 0.001$, and $^{####}P < 0.0001$, compared to the control group.
[d] The ratio of peak intensity between HG-2 group and model group. ↑ Indicates a significant increase in peak intensity and ↓ indicates a significant decrease in peak intensity. $^{*}P < 0.05$, $^{**}P < 0.01$, $^{***}P < 0.001$, and $^{****}P < 0.0001$, compared to the model group. FC: fold change; FA: fatty acid; EETA: epoxyeicosatrienoic acid; HDoHE: hydroxydocosahexaenoic acid; MG: monoglyceride; PC: phosphatidylcholine; PE: phosphatidylethanolamine; PS: phosphatidylserine.

caused surprising improvements in weight, survival rate, lung function, pathological features, and collagen deposition in mice. Thus, different doses (50, 100, and 200 mg/kg) of HG-2 were administered, and found that HG-2 can improve PF indicators, including body weight, lung function, hydroxyproline content, and PF deposition in mice in a dose-dependent manner. We further confirmed the improvement effect of HG-2 on PF at the molecular level. The expression of related proteins in the TGF-β1/Smad pathway, a classical signaling pathway mediating the formation of PF, was detected, and it was found that high doses of HG-2 significantly reduced TGF-β1 levels, Smad2/3 phosphorylation levels, and α-SMA and COL1A1 protein expression levels in the BLM-induced mice lungs, suggesting that HG-2 can improve PF by inhibiting the TGF-β1/Smad pathway. In the same stage, our research group revealed that HG-2 could regulate macrophage polarization by inhibiting TGF-β/Smad pathway to improve PF, which is consistent with the results of this study [38].

HG-2 is a TCM extract with complex chemical components, and its overall efficacy is not the simple addition of a single component but the synergistic effect of multiple components. Therefore, we analyzed the components of HG-2 and performed network pharmacological analysis. We identified 26 components in HG-2, which mainly enriched anthraquinones. Based on compound target prediction, the "HG-2-component-target-IPF" network was constructed, showing that anthraquinones may be the main compound group to exert anti-fibrotic effects. Thin layer chromatography (TLC) analysis showed less anthraquinones were enriched in HG-3 and HG-4, which may be the reason for their weak anti-fibrotic effect (Fig. S5). Rubiadin 1-methyl ether and rubiadin were found to be abundant in HG-2 compared to other compounds and had high binding affinities to targets, which may be the key compounds in the effect of HG-2 in the treatment of PF. PPI network analysis further revealed that HG-2 core targets are associated with tyrosine protein kinases, metalloproteinases, and oxidative inflammation, including EGFR, ERBB2, PDGFRA, PDGFRB, MMP2, MMP9, MAPK1, JAK, JUN, STAT3, PIK3CA, and PTGS2. KEGG enrichment showed that common pathways involved in PF included the HIF-1 signaling pathway, TNF signaling pathway, JAK-STAT signaling pathway, RAS signaling pathway, and MAPK signaling pathway. The expression of growth factors including TGF-β1, platelet-derived growth factor (PDGF), fibroblast growth factor (FGF), and epidermal growth factor (EGF) in lung tissue increased after BLM-induced PF [39]. In addition to the Smad-mediated pathway, TGF-β can activate other signaling cascades, including c-Jun N-terminal kinase (JNK), Ras/

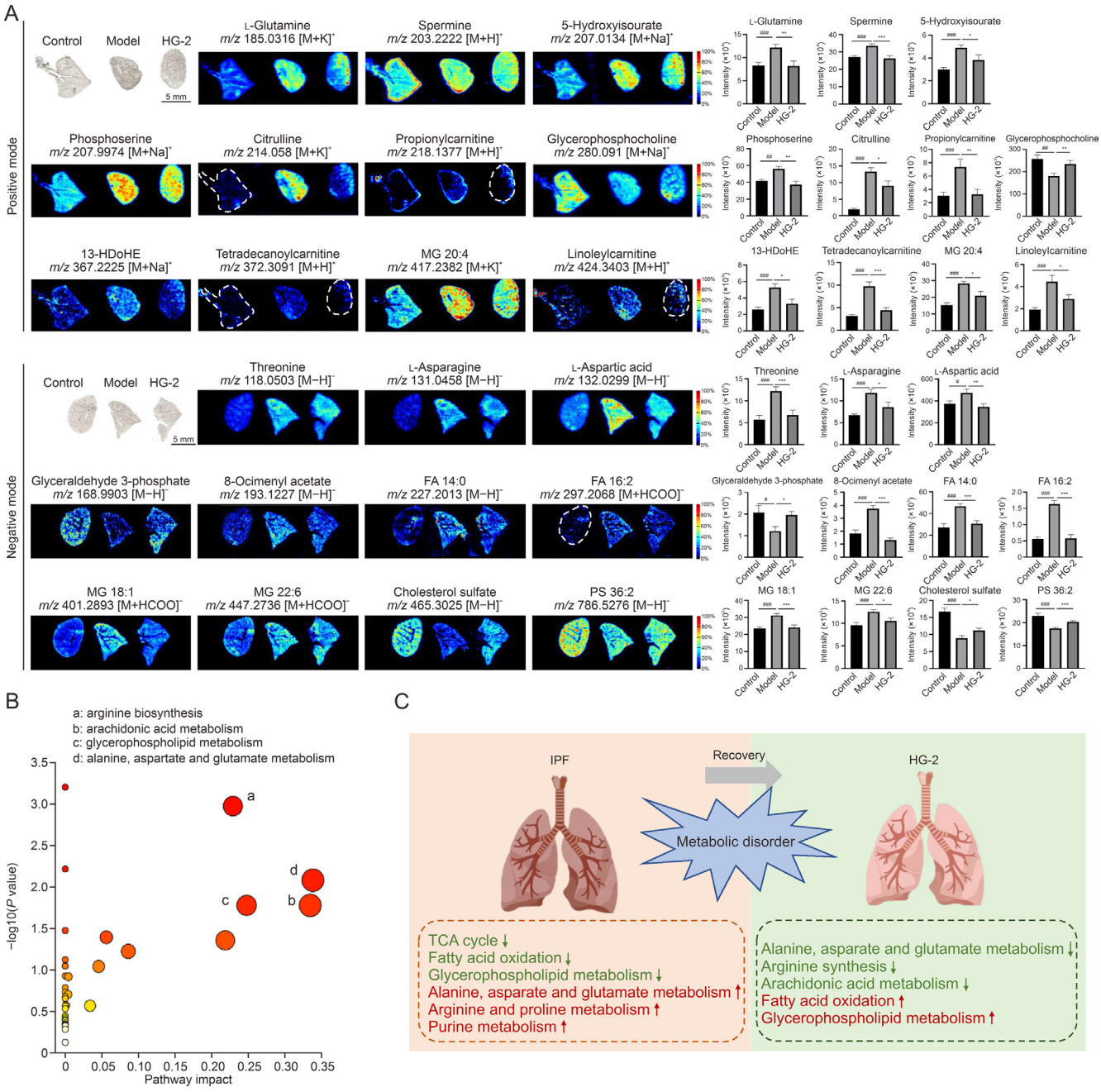

Fig. 8. Visualization of differential metabolites and pathway enrichment analysis of *Prismatomeris connata* Y. Z. Ruan (Huang Gen, HG) ethyl acetate extract (HG-2) treatment in pulmonary fibrosis (PF) mice. (A) Representative mass spectrometry image (MSI) and expression analysis of differential metabolites in mice after bleomycin (BLM) infusion and HG-2 treatment. (B) Pathway enrichment analysis of differential metabolites from Kyoto Encyclopedia of Genes and Genomes (KEGG) database. (C) Changes of PF metabolism after HG-2 administration. All data are expressed as the mean ± standard error of the mean (SEM). $^{\#}P < 0.05$, $^{\#\#}P < 0.01$, and $^{\#\#\#}P < 0.001$, compared to the control group; $^{*}P < 0.05$, $^{**}P < 0.01$, and $^{***}P < 0.001$, compared to the model group. 13-HDoHE: 13-hydroxydocosahexaenoic acid; MG: monoglyceride; FA: fatty acid; PS: phosphatidylserine; IPF: idiopathic PF; TCA: tricarboxylic acid.

MAPK, and p38 MAPK pathways, which also affect the signal transmission of the Smad pathway [40,41]. Related kinases such as MAPK/ mitogen activated protein kinase kinase kinase (MEKK1) can regulate Smad activity and the activation of the Ras/MAPK pathway by TGF-β can positively modulate the TGF-β/Smad pathway [42]. In the pro-inflammatory pathway, the over-expression of pro-inflammatory factors including TNF-α and HIF-1α after fibrosis can activate the corresponding TNF and HIF pathways [43,44]. The JAK/STAT pathway is activated by over-expressed growth factors such as PDGF, FGF, and TGF-β1 [45–47], which also can further activate the HIF-1 pathway [48]. TGF-β also decreased the function of ECM-degrading enzymes and activators (collagenase, MMPs, plasminogen activators, etc.) [49] and MMPs such as MMP1, MMP2, and MMP9 have been proven to be upregulated in the lung tissue or plasma of IPF patients [50,51]. Our results showed that HG-2 may be involved in the regulation of multiple signaling pathways and biological processes, which had significant inhibitory effects on key gene targets such as *PDGFRA*, *PDGFRB, FGFR1*, *MMP2*, *MAPK1*, *JUN,* and *STAT3*.

MSI can realize the qualitative, quantitative, and localization information of metabolites, which is particularly suitable for visualizing the metabolic profile changes of organs in different tissue

micro-regions, thus, elaborating on the relationships between pathophysiological processes and the spatial heterogeneity of metabolites [52–54]. As the main energy organ, the metabolites of the TCA electron transport chain intermediates showed a significant downregulation, and FAs accumulation in the fibrotic lung tissue, suggesting oxidative damage and stress in the mitochondria [55]. In addition, the levels of glutamine-related metabolites were found to be upregulated in PF. The TGF-β-induced increase in glutamine decomposition supports TCA anaplerosis, leading to increased mitochondrial respiration in human lung fibroblasts, which can promote the expression of α-SMA and COL1A2 via energy-dependent contractile activity that is dependent on p38 MAPK [56]. Meanwhile, glutamine decomposition is an important step in collagen synthesis, which can further stimulate the increase in arginine and proline metabolism. Proline is a precursor of collagen synthesis, and the abundance of arginine and the expression level of arginase affect proline synthesis [57]. We found that these amino acids and FAs tended to be highly clustered at the margins of lung tissue, and their abundance was upregulated following fibrosis. We also found an upregulation of purine metabolism and a downregulation of phospholipid metabolism in the lung tissues in BLM-induced PF mice, and those metabolites were widely distributed in the lung parenchyma. In patients with IPF, a large number of abnormally shaped mitochondria were found to accumulate in alveolar type II epithelial cells [58] and the content of phospholipids in bronchial lavage fluid was significantly reduced [59]. Mitochondrial dysfunction and energy deficiency directly affect abnormal epithelial cell function in PF and lead to reduced lipid synthesis [60]. In the absence of energy, ATP produced by purine metabolic pathways may be upregulated as a compensatory mechanism [61].

MSI can also be a potential tool for drug discovery and mechanistic exploration [62], which is used for visualizing the regulation of HG-2 on the overall metabolic network of PF. We found that the metabolic profile of PF can be reversed after HG-2 administration intervention, the contents of amino acids and FAs are potentially reduced, and the contents of phospholipids are potentially increased (Table 2). Oxidative stress plays a vital role in the progression of PF. Network pharmacology analysis showed that HG-2 could regulate cellular responses to reactive oxygen species, involving JNK, Ras/MAPK, and p38 MAPK pathways. During the process of fibrosis, mitochondrial energy metabolism disorders and the upregulation of purine metabolites can produce reactive oxygen species and further induce oxidative stress [43]. In the lipid metabolic reprogramming of PF, the phospholipid metabolites that maintain alveolar surface tension were downregulated, while FAs and arachidonic acid metabolites were upregulated to promote fibrosis by inducing endoplasmic reticulum stress, promoting cell apoptosis, and enhancing the expression of pro-fibrotic biomarkers [63]. HG-2 can improve oxidative stress and inflammation by downregulating arachidonic acid, adenosine, glutamine, and other metabolites and up-regulating phospholipid metabolites. The enrichment of differential metabolite pathways revealed that the mechanism of action of HG-2 may be related to the downregulation of arginine biosynthesis, alanine, asparate and glutamate metabolism, and arachidonic acid metabolism, and the upregulation of glycerolphospholipid metabolism. The integrated approach of network pharmacology and MSI provided a new strategy for the pharmacodynamic evaluation and mechanistic exploration of multi-target drugs. However, further biological verification *in vivo* and *in vitro* is required in the future. Currently, the application of HG-2 in the treatment of PF has obtained the international patent authorization number (PCT/CN2022/086065) [64]. This research provided a new idea for developing drugs to treat PF.

5. Conclusions

In conclusion, this study found a TCM extract, HG-2, with an effective therapeutic effect on BLM-induced PF in mice, which played a multi-target regulatory role by inhibiting the TGF-β1/Smad pathway and the expression of genes for *PDGFR*, *JUN*, *MAPK1*, *MMP2*, and *STAT3*. MSI facilitated the visualization of the heterogeneous distribution of endogenous metabolites in lung tissue and the significant regulatory effect of HG-2 on BLM-induced metabolic disorders in mice. The metabolic regulation mechanism of HG-2 against PF may be closely related to arginine biosynthesis, alanine, asparate and glutamate metabolism, glycerophospholipid metabolism, and arachidonic acid metabolism. This study provided a good starting point for further research on the exact composition and determination of the mechanism of action of HG-2.

CRediT author statement

Haiyan Jiang: Methodology, Investigation, Project administration, Formal analysis, Visualization, Writing - Original draft preparation; **Bowen Zheng:** Investigation, Formal analysis, Visualization; **Guang Hu:** Investigation, Methodology, Project administration, Formal analysis; **Lian Kuang:** Investigation, Validation, Software; **Tianyu Zhou:** Investigation, Formal analysis, Validation; **Sizheng Li:** Investigation, Validation, Writing - Reviewing and Editing; **Xinyi Chen** and **Chuangjun Li:** Resources, Investigation**,** Validation; **Dongming Zhang:** Conceptualization, Resources, Supervision; **Jinlan Zhang:** Conceptualization, Methodology, Supervision; **Zengyan Yang:** Resources, Investigation, Writing - Reviewing and Editing; **Jiuming He:** Conceptualization, Methodology, Supervision, Writing - Reviewing and Editing; **Hongtao Jin:** Conceptualization, Methodology, Project administration, Supervision, Writing - Reviewing and Editing, Funding acquisition.

Declaration of competing interest

The authors declare that there are no conflicts of interest.

Acknowledgments

This study was supported by the National Natural Science Foundation of China (Grant No.: 82074104), the Research Project of Clinical Toxicology Transformation from the Chinese Society of Toxicology, China (Grant No.: CST2021CT101), and the Chinese Academy of Medical Science Innovation Fund for Medical Sciences, China (Grant Nos.: 2017-I2M-1-011 and 2022-I2M-2-002). We would like to thank International Science Editing (http://www.internationalscienceediting.com) for editing this manuscript.

Appendix A. Supplementary data

Supplementary data to this article can be found online at https://doi.org/10.1016/j.jpha.2024.100971.

References

[1] K. Kitowska, D. Zakrzewicz, M. Königshoff, et al., Functional role and species-specific contribution of arginases in pulmonary fibrosis, Am. J. Physiol. Lung Cell Mol. Physiol. 294 (2008) L34–L45.
[2] B. Ley, H.R. Collard, T.E.J. King, Clinical course and prediction of survival in idiopathic pulmonary fibrosis, Am. J. Respir. Crit. Care Med. 183 (2011) 431–440.
[3] G. Raghu, M. Selman, Nintedanib and pirfenidone. New antifibrotic treatments indicated for idiopathic pulmonary fibrosis offer hopes and raises questions, Am. J. Respir. Crit. Care Med. 191 (2015) 252–254.

[4] J. Katzen, M.F. Beers, Contributions of alveolar epithelial cell quality control to pulmonary fibrosis, J. Clin. Investig. 130 (2020) 5088–5099.
[5] D. Wang, B. Deng, L. Cheng, et al., A novel and low-toxic peptide DR3penA alleviates pulmonary fibrosis by regulating the MAPK/miR-23b-5p/AQP5 signaling axis, Acta Pharm. Sin. B 13 (2023) 722–738.
[6] D. Fournier, S. Jouneau, G. Bouzillé, et al., Real-world safety profiles of pirfenidone and nintedanib in idiopathic pulmonary fibrosis patients, Pulm. Pharmacol. Ther. 76 (2022), 102149.
[7] T.M. Dempsey, S. Payne, L. Sangaralingham, et al., Adoption of the antifibrotic medications pirfenidone and nintedanib for patients with idiopathic pulmonary fibrosis, Ann. Am. Thorac. Soc. 18 (2021) 1121–1128.
[8] H. Wu, Y. Yu, H. Huang, et al., Progressive pulmonary fibrosis is caused by elevated mechanical tension on alveolar stem cells, Cell 180 (2020) 107–121. e17.
[9] B. Selvarajah, I. Azuelos, D. Anastasiou, et al., Fibrometabolism – an emerging therapeutic frontier in pulmonary fibrosis, Sci. Signal. 14 (2021), eaay1027.
[10] W. Roque, F. Romero, Cellular metabolomics of pulmonary fibrosis, from amino acids to lipids, Am. J. Physiol. Cell Physiol. 320 (2021) C689–C695.
[11] B. Seeliger, A. Carleo, P.D. Wendel-Garcia, et al., Changes in serum metabolomics in idiopathic pulmonary fibrosis and effect of approved antifibrotic medication, Front. Pharmacol. 13 (2022), 837680.
[12] S. Feng, J. Bai, S. Qiu, et al., Iridoid and phenolic glycosides from the roots of *Prismatomeris connata*, Nat. Prod. Commun. 7 (2012) 561–562.
[13] J. Hao, S. Feng, S. Qiu, et al., Anthraquinone glycosides from the roots of *Prismatomeris connata*, Chin. J. Nat. Med. 9 (2011) 42–45.
[14] S. Feng, Q. Guan, T. Chen, et al., *In vitro* activities of 3-hydroxy-1, 5, 6-trimethoxy-2-methyl-9, 10-anthraquinone against non-small cell lung carcinoma, Arch Pharm. Res. 35 (2012) 1251–1258.
[15] S. Feng, Z. Wang, M. Zhang, et al., HG30, a tetrahydroanthraquinone compound isolated from the roots of *Prismatomeris connate*, induces apoptosis in human non-small cell lung cancer cells, Biomed, Pharmacother. 100 (2018) 124–131.
[16] J. Deng, C. Zhou, Z. Zheng, Protective effect of the alcohol extract from *Prismatomeris tetradra* against liver fibrosis in mice, Lishizhen Med. Mater. Med. Res. 19 (2008) 1339–1341.
[17] Y. Zhang, Z. Yang, J. Li, et al., Chemical constituents in anti-hepatic fibrosis extracts from root of Prismatomeris tetrandra (Roxb.), K. Schum, Chin. J. N. Drugs. 25 (2016) 2868–2870.
[18] Z. Yang, Y. Zhang, J. Li, et al., Metabolites of scopoletin in rat and the effects of drug-containing serum on rat hepatic stellate cells, Chin. J. Comp. Med. 30 (2020) 9–14.
[19] Z. Yang, C. Bai, Q. Zhang, et al., Screening test for effective fraction of against hepatic fibrosis from prismatomerisconnata, Chin. J. Integr. Tradit. West. Med. Liver Dis. 25 (2015) 284–285, 297.
[20] J. He, F. Tang, Z. Luo, et al., Air flow assisted ionization for remote sampling of ambient mass spectrometry and its application, Rapid Commun. Mass Spectrom. 25 (2011) 843–850.
[21] O. Distler, K.B. Highland, M. Gahlemann, et al., Nintedanib for systemic sclerosis-associated interstitial lung disease, N. Engl. J. Med. 380 (2019) 2518–2528.
[22] P. Wei, Y. Xie, P.W. Abel, et al., Transforming growth factor (TGF)-β1-induced miR-133a inhibits myofibroblast differentiation and pulmonary fibrosis, Cell Death Dis. 10 (2019), 670.
[23] D. Chanda, E. Otoupalova, S.R. Smith, et al., Developmental pathways in the pathogenesis of lung fibrosis, Mol. Asp. Med. 65 (2019) 56–69.
[24] S.K. Tirunavalli, M. Kuncha, R. Sistla, et al., Targeting TGF-β/periostin signaling by sesamol ameliorates pulmonary fibrosis and improves lung function and survival, J. Nutr. Biochem. 116 (2023), 109294.
[25] R. Rajesh, R. Atallah, T. Bärnthaler, Dysregulation of metabolic pathways in pulmonary fibrosis, Pharmacol. Ther. 246 (2023), 108436.
[26] E. Bargagli, R.M. Refini, M. D'Alessandro, et al., Metabolic dysregulation in idiopathic pulmonary fibrosis, Int. J. Mol. Sci. 21 (2020), 5663.
[27] Y. Nishioka, S. Homma, T. Okubo, et al., Design of phase 2 study of TAS-115, a novel oral multi-kinase inhibitor, in patients with idiopathic pulmonary fibrosis, Contemp. Clin. Trials Commun. 23 (2021), 100832.
[28] Z.W. Liu, M.Y. Zhao, X.L. Su, et al., The antifibrotic effect and mechanism of a novel tyrosine kinase inhibitor, ZSP1603, in preclinical models of pulmonary fibrosis, Eur. Rev. Med. Pharmacol. Sci. 24 (2020) 1481–1491.
[29] S. Chen, Y. Wei, S. Li, et al., Zanubrutinib attenuates bleomycin-induced pulmonary fibrosis by inhibiting the TGF-β1 signaling pathway, Int. Immunopharmacol. 113 (2022), 109316.
[30] M. Abdalla, L. Thompson, E. Gurley, et al., Dasatinib inhibits TGFβ-induced myofibroblast differentiation through Src-SRF Pathway, Eur. J. Pharmacol. 769 (2015) 134–142.
[31] O. Mammoliti, A. Palisse, C. Joannesse, et al., Discovery of the S1P2 antagonist GLPG2938 (1-[2-Ethoxy-6-(trifluoromethyl)-4-pyridyl]-3-[[5-methyl-6-[1-methyl-3-(trifluoromethyl) pyrazol-4-yl] pyridazin-3-yl] methyl] urea), a preclinical candidate for the treatment of idiopathic pulmonary fibrosis, J. Med. Chem. 64 (2021) 6037–6058.
[32] O. Mammoliti, K. Jansen, S. El Bkassiny, et al., Discovery and optimization of orally bioavailable phthalazone and cinnolone carboxylic acid derivatives as S1P2 antagonists against fibrotic diseases, J. Med. Chem. 64 (2021) 14557–14586.
[33] E.-A. Stylianaki, C. Magkrioti, E.M. Ladopoulou, et al., "Hit" to lead optimization and chemoinformatic studies for a new series of Autotaxin inhibitors, Eur. J. Med. Chem. 249 (2023), 115130.
[34] H. Lei, Z. Cao, H. Wu, et al., Structural and PK-guided identification of indole-based non-acidic autotaxin (ATX) inhibitors exhibiting high *in vivo* anti-fibrosis efficacy in rodent model, Eur. J. Med. Chem. 227 (2022), 113951.
[35] T.M. Maher, P. Ford, K.K. Brown, et al., Ziritaxestat, a novel autotaxin inhibitor, and lung function in idiopathic pulmonary fibrosis: the ISABELA 1 and 2 randomized clinical trials, JAMA 329 (2023) 1567–1578.
[36] M.L. Decaris, J.R. Schaub, C. Chen, et al., Dual inhibition of αvβ6 and αvβ1 reduces fibrogenesis in lung tissue explants from patients with IPF, Respir. Res. 22 (2021), 265.
[37] Y. Huang, J. Deng, Y. Tian, et al., Mangostanin derivatives as novel and orally active phosphodiesterase 4 inhibitors for the treatment of idiopathic pulmonary fibrosis with improved safety, J. Med. Chem. 64 (2021) 13736–13751.
[38] S. Li, G. Hu, L. Kuang, et al., Unraveling the mechanism of ethyl acetate extract from *Prismatomeris connata* Y. Z. Ruan root in treating pulmonary fibrosis: Insights from bioinformatics, network pharmacology, and experimental validation, Front. Immunol. 14 (2024), 1330055.
[39] J.C. Hewlett, J.A. Kropski, T.S. Blackwell, Idiopathic pulmonary fibrosis: epithelial-mesenchymal interactions and emerging therapeutic targets, Matrix Biol. 71–72 (2018) 112–127.
[40] R. Derynck, Y. Zhang, Smad-dependent and Smad-independent pathways in TGF-β family signalling, Nature 425 (2003) 577–584.
[41] M. Kretzschmar, J. Doody, I. Timokhina, et al., A mechanism of repression of TGFbeta/Smad signaling by oncogenic Ras, Genes Dev. 13 (1999) 804–816.
[42] K.M. Mulder, Role of Ras and Mapks in TGFbeta signaling, Cytokine Growth Factor Rev. 11 (2000) 23–35.
[43] P. Saha, P. Talwar, Idiopathic pulmonary fibrosis (IPF): disease pathophysiology, targets, and potential therapeutic interventions, Mol. Cell. Biochem. 2023. https://doi.org/10.1007/s11010-023-04845-6.
[44] H. Xie, J.-T. Tan, R.-L. Wang, et al., Expression and significance of HIF-1α in pulmonary fibrosis induced by paraquat, Exp. Biol. Med. (Maywood) 238 (2013) 1062–1068.
[45] J. Milara, G. Hernandez, B. Ballester, et al., The JAK2 pathway is activated in idiopathic pulmonary fibrosis, Respir. Res. 19 (2018), 24.
[46] H. Ruan, J. Luan, S. Gao, et al., Fedratinib attenuates bleomycin-induced pulmonary fibrosis via the JAK2/STAT3 and TGF-β1 signaling pathway, Molecules 26 (2021), 4491.
[47] P. Montero, J. Milara, I. Roger, et al., Role of JAK/STAT in interstitial lung diseases; molecular and cellular mechanisms, Int. J. Mol. Sci. 22 (2021), 6211.
[48] Z. Luo, M. Tian, G. Yang, et al., Hypoxia signaling in human health and diseases: implications and prospects for therapeutics, Signal Transduct. Target. Ther. 7 (2022), 218.
[49] A.D. Widgerow, Chronic wounds – is cellular 'reception' at fault? Examining integrins and intracellular signalling, Int. Wound J. 10 (2013) 185–192.
[50] V.J. Craig, L. Zhang, J.S. Hagood, et al., Matrix metalloproteinases as therapeutic targets for idiopathic pulmonary fibrosis, Am. J. Respir. Cell Mol. Biol. 53 (2015) 585–600.
[51] A. Pardo, S. Cabrera, M. Maldonado, et al., Role of matrix metalloproteinases in the pathogenesis of idiopathic pulmonary fibrosis, Respir. Res. 17 (2016), 23.
[52] J. Chen, Y. Wang, J. Ko, Single-cell and spatially resolved omics: advances and limitations, J. Pharm. Anal. 13 (2023) 833–835.
[53] Y. Zhou, X. Jiang, X. Wang, et al., Promise of spatially resolved omics for tumor research, J. Pharm. Anal. 13 (2023) 851–861.
[54] X. Wang, J. Zhang, K. Zheng, et al., Discovering metabolic vulnerability using spatially resolved metabolomics for antitumor small molecule-drug conjugates development as a precise cancer therapy strategy, J. Pharm. Anal. 13 (2023) 776–787.
[55] B. Shan, H. Zhou, C. Guo, et al., Tanshinone IIA ameliorates energy metabolism dysfunction of pulmonary fibrosis using ^{13}C metabolic flux analysis, J. Pharm. Anal. 14 (2024) 244–258.
[56] K. Bernard, N.J. Logsdon, S. Ravi, et al., Metabolic reprogramming is required for myofibroblast contractility and differentiation, J. Biol. Chem. 290 (2015) 25427–25438.
[57] M. Endo, S. Oyadomari, Y. Terasaki, et al., Induction of arginase I and II in bleomycin-induced fibrosis of mouse lung, Am. J. Physiol. Lung Cell Mol. Physiol. 285 (2003) L313–L321.
[58] M. Bueno, Y.C. Lai, Y. Romero, et al., PINK1 deficiency impairs mitochondrial homeostasis and promotes lung fibrosis, J. Clin. Investig. 125 (2015) 521–538.
[59] P.C. Robinson, L.C. Watters, T.E. King, et al., Idiopathic pulmonary fibrosis. Abnormalities in bronchoalveolar lavage fluid phospholipids, Am. Rev. Respir. Dis. 137 (1988) 585–591.
[60] C.W. Agudelo, G. Samaha, I. Garcia-Arcos, Alveolar lipids in pulmonary disease. A review, Lipids Health Dis. 19 (2020), 122.
[61] O.D. Maddocks, C.F. Labuschagne, P.D. Adams, et al., Serine metabolism supports the methionine cycle and DNA/RNA methylation through de novo ATP synthesis in cancer cells, Mol. Cell 61 (2016) 210–221.
[62] H. Pang, Z. Hu, Metabolomics in drug research and development: the recent advances in technologies and applications, Acta Pharm. Sin. B 13 (2023) 3238–3251.
[63] R. Chen, J. Dai, Lipid metabolism in idiopathic pulmonary fibrosis: from pathogenesis to therapy, J. Mol. Med. 101 (2023) 905–915.
[64] H. Jin, J. Zhang, G. Hu, et al., Inventors; A pharmaceutical composition for preventing and treating lung injury, a preparation method and its application, International patent PCT/CN2022/086065, 4 November 2022.